remote sensing

Article

Analysis of Environmental and Atmospheric Influences in the Use of SAR and Optical Imagery from Sentinel-1, Landsat-8, and Sentinel-2 in the Operational Monitoring of Reservoir Water Level

Wendson de Oliveira Souza [1], Luis Gustavo de Moura Reis [2], Antonio Miguel Ruiz-Armenteros [3,4,5,*], Doris Veleda [6], Alfredo Ribeiro Neto [2], Carlos Ruberto Fragoso Jr. [7], Jaime Joaquim da Silva Pereira Cabral [2,8] and Suzana Maria Gico Lima Montenegro [2]

[1] Department of Transports, Center for Technology, Federal University of Piauí (UFPI), Teresina 64049-550, Brazil; wendsonsouza@ufpi.edu.br
[2] Center for Technology and Geosciences, Federal University of Pernambuco (UFPE), Recife 50670-901, Brazil; luis.gustavoreis@ufpe.br (L.G.d.M.R.); alfredo.ribeiro@ufpe.br (A.R.N.); jaime.cabral@ufpe.br (J.J.d.S.P.C.); suzanam@ufpe.br (S.M.G.L.M.)
[3] Department of Cartographic, Geodetic and Photogrammetry Engineering, University of Jaén, Campus Las Lagunillas s/n, 23071 Jaén, Spain
[4] Microgeodesia Jaén Research Group (PAIDI RNM-282), University of Jaén, Campus Las Lagunillas s/n, 23071 Jaén, Spain
[5] Center for Advanced Studies on Earth Sciences, Energy and Environment CEACTEMA, University of Jaén, Campus Las Lagunillas s/n, 23071 Jaén, Spain
[6] Renewable Energy Center (CER), Laboratory of Physical, Coastal, and Estuarine Oceanography (LOFEC), Federal University of Pernambuco (UFPE), Recife 50740-550, Brazil; doris.veleda@ufpe.br
[7] Center for Technology (CTEC), Federal University of Alagoas (UFAL), Maceió 57072-970, Brazil; ruberto@ctec.ufal.br
[8] Department of Civil Engineering, Polytechnic School, University of Pernambuco (UPE), Recife 50720-001, Brazil
* Correspondence: amruiz@ujaen.es

Abstract: In this work, we aim to evaluate the feasibility and operational limitations of using Sentinel-1 synthetic aperture radar (SAR) data to monitor water levels in the Poço da Cruz reservoir from September 2016–September 2020, in the semi-arid region of northeast Brazil. To segment water/non-water features, SAR backscattering thresholding was carried out via the graphical interpretation of backscatter coefficient histograms. In addition, surrounding environmental effects on SAR polarization thresholds were investigated by applying wavelet analysis, and the Landsat-8 and Sentinel-2 normalized difference water index (NDWI) and modified normalized difference water index (MNDWI) were used to compare and discuss the SAR results. The assessment of the observed and estimated water levels showed that (i) SAR accuracy was equivalent to that of NDWI/Landsat-8; (ii) optical image accuracy outperformed SAR image accuracy in inlet branches, where the complexity of water features is higher; and (iii) VV polarization outperformed VH polarization. The results confirm that SAR images can be suitable for operational reservoir monitoring, offering a similar accuracy to that of multispectral indices. SAR threshold variations were strongly correlated to the normalized difference vegetation index (NDVI), the soil moisture variations in the reservoir depletion zone, and the prior precipitation quantities, which can be used as a proxy to predict cross-polarization (VH) and co-polarization (VV) thresholds. Our findings may improve the accuracy of the algorithms designed to automate the extraction of water levels using SAR data, either in isolation or combined with multispectral images.

Keywords: hydrological analysis; multi-sensors; time series; Sentinel-1; Sentinel-2; Landsat-8; reservoir; monitoring

check for updates

Citation: Souza, W.d.O.; Reis, L.G.d.M.; Ruiz-Armenteros, A.M.; Veleda, D.; Ribeiro Neto, A.; Fragoso Jr., C.R.; Cabral, J.J.d.S.P.; Montenegro, S.M.G.L. Analysis of Environmental and Atmospheric Influences in the Use of SAR and Optical Imagery from Sentinel-1, Landsat-8, and Sentinel-2 in the Operational Monitoring of Reservoir Water Level. *Remote Sens.* **2022**, *14*, 2218. https://doi.org/10.3390/rs14092218

Academic Editors: Hyongki Lee, Joong-Sun Won, Sanggyu Lee and Euiho Hwang

Received: 22 March 2022
Accepted: 2 May 2022
Published: 5 May 2022

1. Introduction

Monitoring and mapping surface water features and their spatial- and temporal-scale distribution are of great importance for understanding hydrological processes and supporting water resource management [1]. For this purpose, remote sensing can provide timely and cost-effective information, considering the high variability in both space and time of hydrological features, which is necessary in order to monitor and characterize their dynamics [2] at global and regional scales.

Over time, water body extraction methods have been applied almost exclusively over multispectral satellite imagery due to their accessibility, ease, and straightforward interpretation. See, for instance [3]: the thematic classification method [4–6], the linear unmixing model [7,8], the single-band thresholding method [9,10], and the spectral water index method [11–18], among others. Approaches involving the combination of different methods have also been proposed [19,20], as well as the construction of decision trees [21,22] to improve the reliability in the process of surface water collection.

Among these methods, water indices are the most commonly used because of their ease of use, efficiency, and low operational costs [23]. These include the normalized difference water index (NDWI) [11] and the modified normalized difference water index (MNDWI) [12]. The former uses green and near-infrared (NIR) reflectance bands to suppress soil and vegetation noise in the water extraction process. MNDWI, on the other hand, uses the shortwave infrared (SWIR) band instead of the NIR band used in NDWI. By doing this, the MNDWI captures more subtle water characteristics more stably and reliably, enhancing its ability to suppress the buildup of noise [12,24,25]. Although many water extraction methods based on multispectral imagery are available, they are subject to operational limitations. Optical satellite imagery can only be used under favorable weather conditions [26,27].

Even with several SAR satellites available [28], for many years, access to data remained limited to a few users due to the high costs and the need to have specific knowledge and software in order to perform image processing and interpretation. However, in recent years, SAR products have been democratized thanks to the Copernicus program, resulting from a partnership between the European Space Agency (ESA) and the European Commission (EC). This service provides Earth observation products free of charge through six satellite missions, called Sentinels. Among them, Sentinel-1 stands out, operating with a SAR instrument aimed at land monitoring.

In operation since 2014, Sentinel-1 has had a growing presence in the detection of surface water. Its spatial resolution and short temporal baselines are essential features for the extraction of water bodies. They also facilitate the monitoring of the changes in water sources, which are dynamic in space and time [29]. Consequently, the new SAR system is recurrently being used in flood mapping [30], delimiting wetlands [31], and reservoir monitoring [32]. Despite the advantages mentioned above, especially the all-weather capability, SAR data can be affected by physical environmental conditions, such as rain, wind [2], soil moisture [33], and seasonal landcover patterns [34], which affect the amount of energy backscattered in each polarization band.

Furthermore, several studies have been dedicated to improving water extraction using the threshold approach with SAR observation data, for instance, the use of multiple local thresholds appropriate to each land type [35,36]. In addition, despite the well-known sensitivity of active and passive microwaves to variations in the dielectric constant of the soil surface [37–40] and hence soil moisture, their relationship with the backscatter threshold is still understudied.

Furthermore, empirical approaches in water extraction tasks, which are capable of predicting the threshold backscatter coefficient considering other variables related to soil moisture content, such as precipitation and vegetation health signal, are of great importance for practical and operational purposes. This is especially important when considering the complexity of employing physically theoretical models, such as the integral equation method [41], which applies electromagnetic scattering theory to the soil surface.

In this work, we aim to investigate the feasibility of employing Sentinel-1 SAR imagery for the operational monitoring of the Poço da Cruz reservoir in Pernambuco State (Brazil), and the influence of environmental factors, such as precipitation, soil moisture, and vegetation vigor, on the backscattering signal. The performance analysis also considered additional elements: data availability, SAR polarization, reservoir storage level, land use interactions, and water indices from different optical sensors.

The results of the water feature extraction from Sentinel-1 SAR data showed similar accuracy to that of NDWI/Landsat-8 and lower accuracy than NDWI/Sentinel-2 and MNDWI (Landsat-8 and Sentinel-2) data. From September 2016 to the beginning of October 2020, 71% of the images from the Landsat-8 and Sentinel-2 satellites were unable to be used due to atmospheric effects and poor weather conditions, which hampers the usability of optical sensors. We offer more elements to maximize the combined use of SAR and optical sensors, aiming to enhance the operational monitoring of water features using remote sensing.

2. Materials and Methods

2.1. Study Area

The study area consisted of the 'Poço da Cruz' (PC) reservoir (Figure 1), a public dam located in Ibimirim municipality, Pernambuco State, northeastern Brazil. It is the largest reservoir in the state, with a storage capacity of 504 hm^3 and a hydraulic basin of approximately 62 km^2, as well as maximum and minimum water levels of 421.7 and 435 m, respectively. Commissioned in the early 1960s by the National Department of Works Against Drought (DNOCS), the reservoir provides water for irrigation, fish farming, and energy generation. The hydrological regime of accumulation is characterized by an annual accumulation cycle; therefore, the reservoir water levels are not related to the current seasonal inflow. According to the National Meteorological Institute of Brazil (INMET), the annual average precipitation is 421.8 mm, which is typical of semi-arid regions, concentrated in the six-month period from December to May. March is usually the rainiest month, and September is the driest. The mean local wind velocity is 3.1 m/s, with a maximum of 3.87 m/s in September and a minimum of 2.2 m/s in March (monthly average values).

The reservoir neighborhood landscape contains the following features: caatinga vegetation, pasture, bare soil, agriculture, and rural infrastructure. In the caatinga biome, the vegetation health is characterized by seasonality, which is typical of semi-arid areas, the vigor of which is strongly correlated with prior precipitation incidence.

The depletion zone is an important soil feature that is present in most of the reservoir's perimeter. It is covered by water during high storage periods, but during periods of low storage, rocks, sand, and bare soil are exposed, and this area is partially occupied by undergrowth, pasture, or agriculture during the rainy season.

In the reservoir inlet branches, where agriculture is more concentrated and the depths are shallower, the level of nutrients and chlorophyll concentrations are higher, leading to the presence of macrophyte vegetation over water.

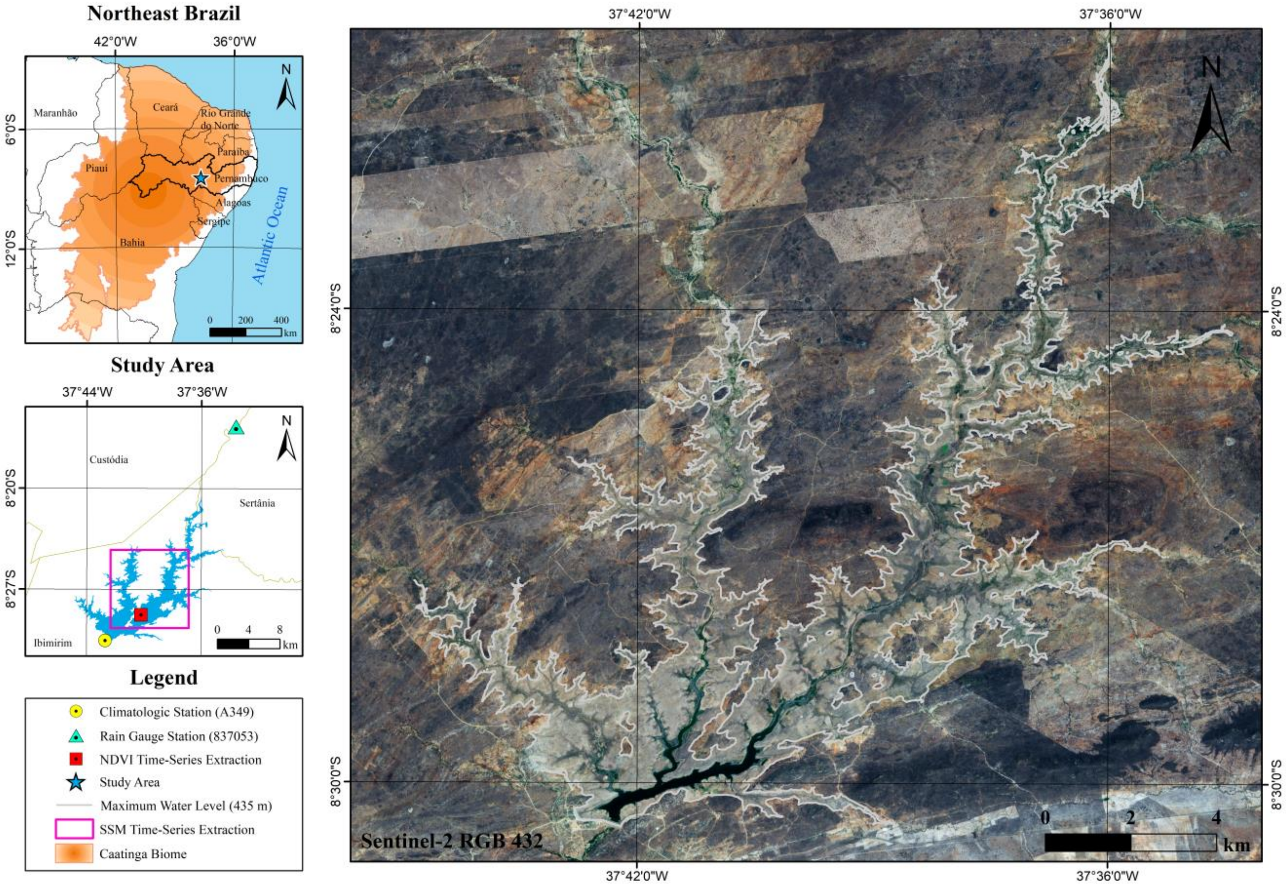

Figure 1. Location map of the Poço da Cruz reservoir, Pernambuco, Brazil.

2.2. Dataset

2.2.1. SAR Data Pre-Processing

The Sentinel-1 images were downloaded from the ESA-EC Copernicus Open Access Hub (https://scihub.copernicus.eu/dhus), consisting of 122 SAR products covering a period from 30 September 2016 to 21 September 2020. Their characteristics are summarized in Table 1.

Table 1. Sentinel-1 data specifications.

Satellite platform	Sentinel-1A
Frequency	5.405 GHz (C-band)
Product type	Ground Range Detected (GRD)
Sensor mode	Interferometric Wide Swath (IW)
Sub-swath	IW1
Polarization	Dual (VV and VH)
Pass direction	Descending
Spatial resolution	20.4 m × 22.5 m (range × azimuth)
Incidence angle	32.9°
Swath width	251.8 km
Temporal resolution	12 days
Relative orbit number	82

SAR images were pre-processed with the Sentinel-1 Toolbox (S1TBX) in the Sentinel Application Platform (SNAP) to generate calibrated and orthorectified products. Accordingly to Filipponi [42], the processing chain illustrated in Figure 2 includes the following steps: updating of orbit metadata with precise orbit files; removal of additive noise in sub-bands to reduce discontinuity in the acquisition of several bands; removal of low-intensity noise and invalid data at the edges of the area; radiometric calibration using the sensor calibration parameters in the metadata; use of the Lee filter with a 5 × 5 pixel window to filter speckle; and correction of the geometry of the terrain from the 1-arcsec SRTM DEM, with corrected values of the surface terrain converted into decibels (dB) using logarithmic transformation.

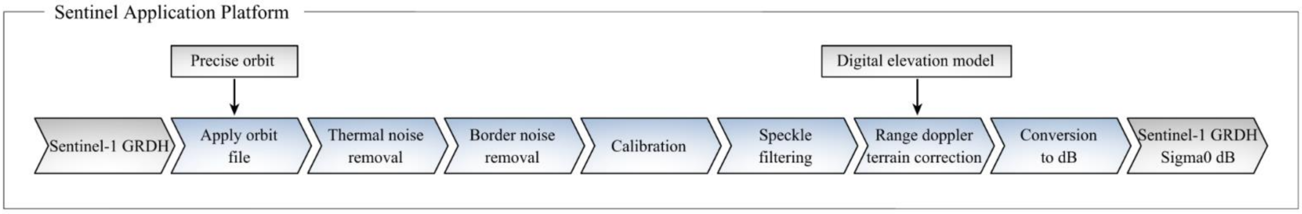

Figure 2. Sentinel-1 data preprocessing steps.

The images obtained through this process were transformed into SIRGAS2000 data (Geocentric Reference System for the Americas, in the year 2000), projected in Universal Transverse Mercator (UTM), Zone 24 south, and resampled to 10 m spatial resolution.

It is known that stress caused by wind over the water surface can broaden the backscattering signal. This mechanism is known as Bragg resonance and occurs when the component of wave spectra resonates with the radar wavelength. For C band radar imagery, the wind speed threshold is estimated to be 3.25 m/s at 10 m above the surface [43].

A preliminary analysis of mean wind velocity over INMET climatological station A349 data (Figure 1) in the study area showed that of the 122 SAR images, 43.4% were taken under unfavorable wind conditions, with a wind velocity higher than the threshold mentioned above (Figure 3). Nevertheless, no SAR data were discarded for this reason since water body delimitation was performed via graphical interpretation, as described in Section 2.5. In this approach, the borderline delimitation is more important than the correct water pixel classification inside the reservoir water surface once the water elevation has been obtained via the use of a high-resolution digital elevation model (DEM). As the main objective of this study was to evaluate the SAR operational capability, continuous data availability was one of the most crucial prerequisites, and the occurrence of winds higher than 3.25 m/s was a probable event, considering the local wind climatology.

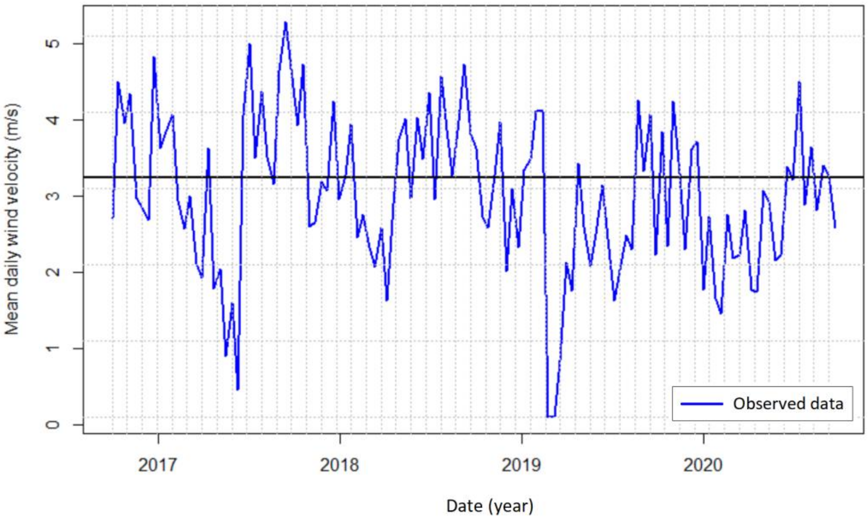

Figure 3. Mean daily wind velocity in SAR image dates. Source: INMET climatological station A349.

2.2.2. Multispectral Image Pre-Processing

The Google Earth Engine (GEE, https://earthengine.google.com), a cloud-based platform for geospatial processing [44], was used to obtain 75 Landsat-8/OLI (Operational Land Imager) images from 29 September 2016 to 24 September 2020 and 236 Sentinel-2/MSI (Multi-Spectral Instrument) images from 18 September 2016 to 2 October 2020. The specifications of both products are shown in Table 2.

Table 2. Landsat-8 and Sentinel-2 image specifications.

Satellite (Sensor)	Band	Wavelength (µm)	Level/ Correction	Spatial Resolution (m)	Temporal Resolution (Days)
Landsat-8 (OLI)	Green	0.530–0.590	Tier 1 only	30	16
	NIR	0.850–0.880			
	SWIR	1.570–1.650			
Sentinel-2 (MSI)	Green	0.560 (S2A)/0.559 (S2B)	L1C/TOA	10 and 20	5
	NIR	0.835 (S2A)/0.833 (S2B)		10	
	SWIR	1.613 (S2A)/1.610 (S2B)		20	

Note: L1C is orthorectified top-of-atmosphere (TOA) reflectance.

Regarding multispectral data, 49 (65%) of the 75 Landsat-8 and 182 (77%) of the 236 Sentinel-2 available scenes were affected by atmospheric conditions (clouds, shadows), preventing their use in this study (Figure 4). After discarding cloudy data, only 80 images were effectively available: 26 Landsat-8 and 54 Sentinel-2.

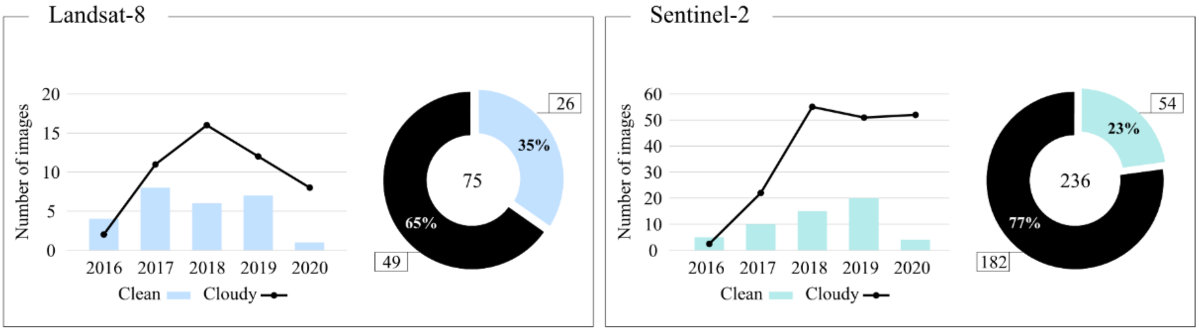

Figure 4. Multispectral Landsat-8 and Sentinel-2 images affected by atmospheric conditions from September 2016 to early October 2020.

Pre-processing (Figure 5) was performed on the green, NIR, and SWIR bands of the Landsat-8/OLI and Sentinel-2/MSI data with the application of the methods NDWI [11], Equation (1), and MNDWI [12] according to Equation (2). The water index images were then converted into the SIRGAS2000 geodetic coordinate system and gridded into UTM zone 24 south. For water extraction, NDWI and MNDWI pixel values greater than or equal to zero were denoted as water.

$$\mathrm{NDWI} = \frac{\rho_{\mathrm{Green}} - \rho_{\mathrm{NIR}}}{\rho_{\mathrm{Green}} + \rho_{\mathrm{NIR}}} \tag{1}$$

$$\mathrm{MNDWI} = \frac{\rho_{\mathrm{Green}} - \rho_{\mathrm{SWIR}}}{\rho_{\mathrm{Green}} + \rho_{\mathrm{SWIR}}} \tag{2}$$

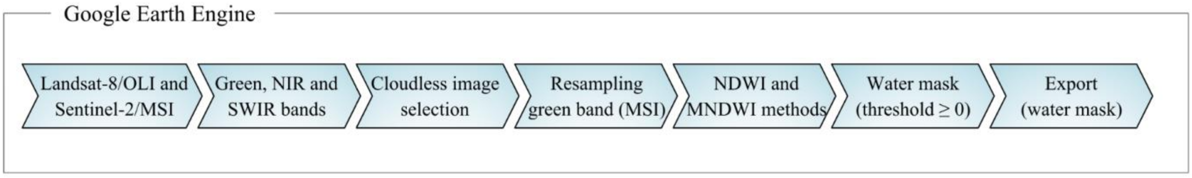

Figure 5. Multispectral pre-processing steps for multispectral images.

2.2.3. Digital Elevation Model

The digital elevation model (DEM) of the PC reservoir was provided by the Brazilian Water Agency (ANA) and consisted of an aerial laser survey, using LiDAR (Light Detection and Ranging) technology for the land part integrated with a bathymetric survey for the flooded area. The latter was carried out with an eco-probe using a single beam for shallow waters with depths less than 5 m and a multibeam for deep waters. Both were referenced to the Brazilian Geodetic System (SGB), resulting in a 1 m spatial resolution image, with values ranging from 403.16 m to 435.90 m (spillway dam) [45].

2.3. SAR Backscattering Thresholding

The SAR backscattering intensity was analyzed to map water features by means of negative values, referring to water pixel characteristics. These aspects stem from the fact that surface waters can act as mirrors and reflect almost all incoming energy in the specular direction [46]. Therefore, they present extremely low backscatter intensity compared to most land or vegetation features.

Based on this physical principle, thresholding was conducted in a supervised manner in the SNAP based on the bimodal histogram distribution of the SAR backscatter coefficient σ°. A graphical interpretation was carried out for each Sentinel-1A SAR image to select the best threshold for discriminating water from non-water features (Figure 6).

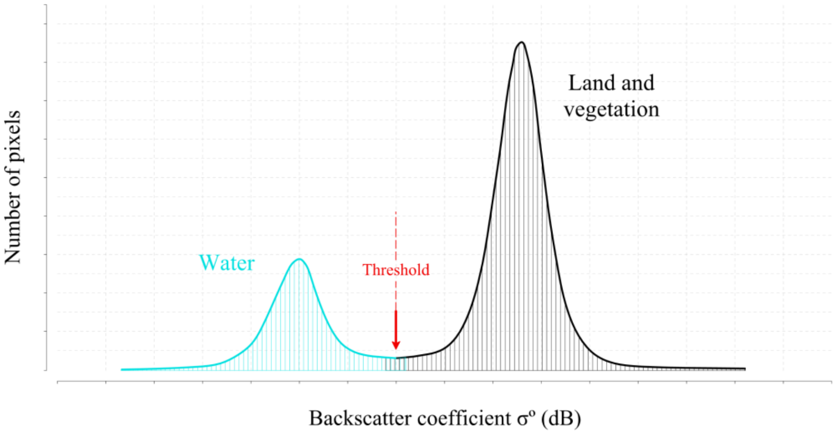

Figure 6. Example of a histogram of SAR backscatter intensity.

Based on the SAR backscatter coefficient histograms of each image, the water segmentation threshold was adjusted via graphical interpretation, seeking to minimize noise and maximize water area (see an example in Figure 7).

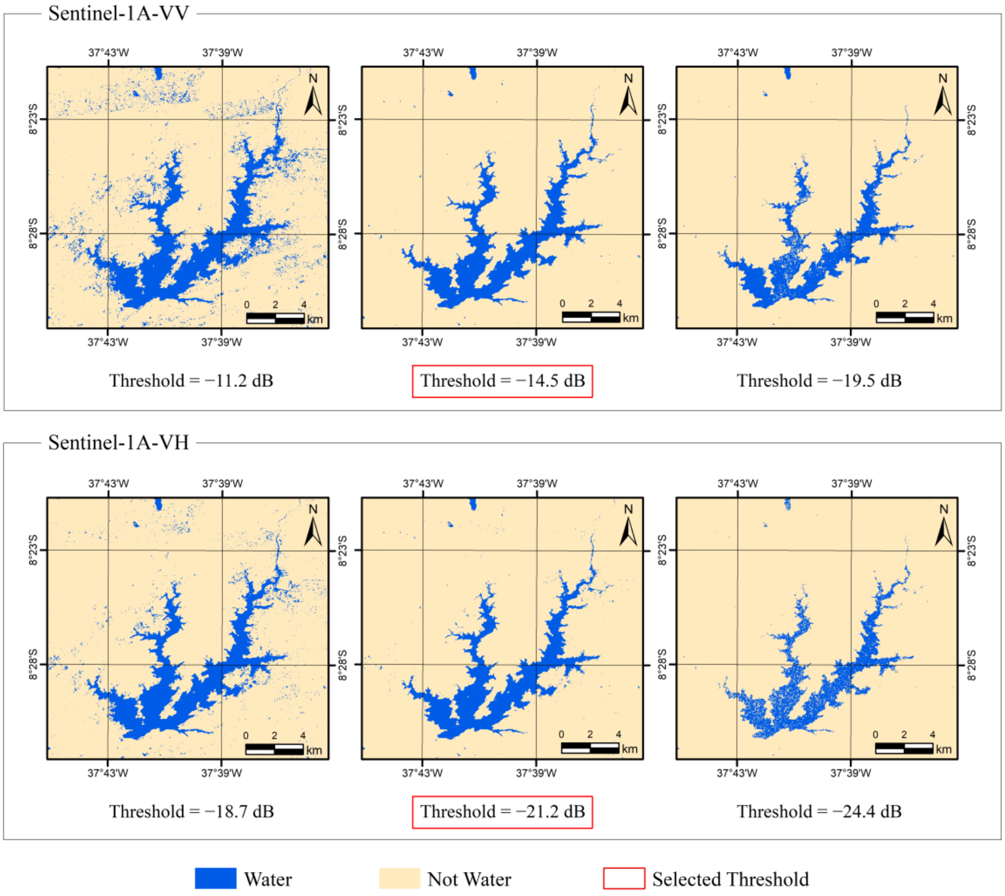

Figure 7. Water segmentation threshold variation for the date 5 June 2020.

2.4. *SAR Physical Environmental Influences over Backscattering Thresholding*

Understanding physical environmental effects on the adjusted VV and VH backscattering thresholds are of great importance for evaluating SAR operational monitoring capability. VV is the linear co-polarized band and has the same transmitted and received polarizations. VH is cross-polarized and has orthogonal transmitted and received polarizations. For this purpose, the relationship between the backscattering thresholds and the variables of precipitation, vegetation health signal, and soil moisture were investigated. These variables were known to play an essential role in SAR backscattering mechanisms due to their sensitivity to surface properties, especially dielectric constant and roughness [37,39].

The precipitation (P) data were obtained from rain gauge station 837053, administered by the Brazilian Water Agency (ANA) and situated approximately 10 km northeast of the dam site (Figure 1), once the INMET climatological station data (A349) were unavailable for the period of interest.

The vegetation health signal was taken from the normalized difference vegetation index (NDVI), calculated using the MODIS/TERRA sensor images through the Vegetation Temporal Analysis System (SATVeg) [47]. The product includes 16-day image composites, with a spatial resolution of 250 m and geometric, radiometric, and atmospheric correction levels [48]. Four pixels centered at latitude −8.48° and longitude −37.67° (Figure 1) were chosen to extract the NDVI time series from 29 September 2016 to 6 March 2021.

Surface soil moisture (SSM) was obtained from the NASA-USDA SMAP Global soil moisture information. Soil Moisture Active Passive (SMAP) is a satellite mission launched in January 2015 that employs L-band radar and radiometer instruments. The product has a 10 km spatial resolution and 3-day composites, available since 1 April 2015. The SSM time series was obtained through GEE at latitude −8.45° and longitude −37.66°.

To investigate the main factor affecting the backscattering changes in our study area and to provide insights to develop future empirically derived models, the variables and their relationships were analyzed using wavelets by means of the following methods: continuous wavelet transformation (CWT) and wavelet transform coherence (WTC). A wavelet is a powerful tool for analyzing non-stationary processes. It decomposes a time series in the frequency-time domain and identifies intermittent oscillations for different periodicities [49]. To analyze the common power relationship between two variables, we used WTC, which detects transient but significant coherence between two nonlinear signals. Maraun and Kurths [50] suggest applying WTC for the simultaneous analysis of two signals instead of the cross-wavelet approach, which can show misleading peaks if only one of the time series exhibits strong peaks. Accordingly, in this work, we applied WTC to identify causality relationships between two signals at frequency bands and time intervals. These methods are appropriate for studying two time series together in pairs, and examining causality relationships in time space-frequency [49]. The coherence phase, represented by arrows, shows the lead/lag phase relations between the series. It can be interpreted as follows: when the phase arrows point to the right, it means that the series is in phase, to the left means that they are in anti-phase, to the right-down or left-up indicate that the first variable is leading, whereas arrows pointing to the right-up or left-down mean that the second variable is leading. The analyses of transformations were carried out using the R package biwavelet [51]. Due to the difference in acquisition frequency, NDVI and SSM data were linearly interpolated to match the frequencies of the SAR dates.

After identifying regions in the time-frequency domain of wavelet spectra where the variables co-varied with a strong association, the time series were accumulated for P, averaged for NDVI and SSM, and plotted against VV and VH backscattering thresholds, to evaluate their linear correlation.

2.5. Assessment of Water Level

Surface water features extracted from SAR and multispectral images were used to estimate the water level. The DEM provided by ANA was used at this step. The process was carried out in six steps (Figure 8): (i) conversion of the water mask from products (SAR and optical) into a vector element (polygon geometry); (ii) removal of noisy polygons outside the maximum limits of the DEM; (iii) vector transformation of polygon geometry to points; (iv) extraction of water level information from point intersections with the DEM; (v) water levels were assumed to be the mean (Me), median (Mn), and mode (Mo), calculated from the extracted water elevation dataset values; and (vi) assessment of reservoir water elevation in each scene.

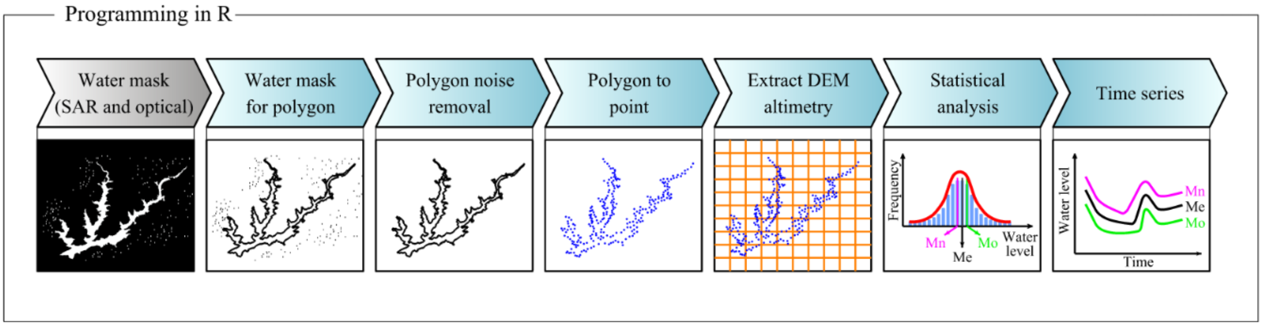

Figure 8. Workflow illustrating the water level estimation process.

The process described above was automated through geoprocessing scripts developed in the R programming language, using the R packages raster [52], ggplot2 [53], and Sf [54].

The daily observed water level was used to evaluate the accuracy of the water level estimations. The observed data were provided by the Water and Climate Agency of Pernambuco state (APAC), starting on 1 July 2000 and were converted to the SGB format by adding 0.9 m. Due to the gaps in water level observations and cloudy multispectral scenes, only 61 Sentinel-1 images (Table 3), 12 Landsat-8, and 32 Sentinel-2 (Table 4) were employed in the accuracy assessment.

Table 3. Sentinel-1 imagery dataset used to assess accuracy.

Satellite	No. of Images	Date
Sentinel-1	61	28/01/2017, 09/02/2017, 31/10/2017, 28/02/2018, 24/03/2018, 05/04/2018, 17/04/2018, 28/06/2018, 10/07/2018, 22/07/2018, 03/08/2018, 15/08/2018, 27/08/2018, 08/09/2018, 20/09/2018, 02/10/2018, 14/10/2018, 26/10/2018, 07/11/2018, 19/11/2018, 01/12/2018, 13/12/2018, 25/12/2018, 06/01/2019, 18/01/2019, 30/01/2019, 11/02/2019, 23/02/2019, 07/03/2019, 19/03/2019, 31/03/2019, 12/04/2019, 24/04/2019, 11/06/2019, 23/06/2019, 05/07/2019, 17/07/2019, 29/07/2019, 10/08/2019, 22/08/2019, 03/09/2019, 15/09/2019, 27/09/2019, 09/10/2019, 21/10/2019, 02/11/2019, 14/11/2019, 08/12/2019, 20/12/2019, 01/01/2020, 13/01/2020, 25/01/2020, 06/02/2020, 18/02/2020, 12/05/2020, 24/05/2020, 05/06/2020, 17/06/2020, 29/06/2020, 11/07/2020, 23/07/2020

Table 4. Landsat-8 and Sentinel-2 imagery datasets used to assess accuracy.

Satellite	No. of Images	Date
Landsat-8	12	19/11/2017, 01/07/2018, 17/07/2018, 21/10/2018, 08/12/2018, 25/01/2019, 14/03/2019, 02/06/2019, 21/08/2019, 24/10/2019, 11/12/2019, 27/12/2019
Sentinel-2	32	26/01/2017, 21/05/2018, 20/07/2018, 30/07/2018, 04/08/2018, 14/08/2018, 23/09/2018, 23/10/2018, 28/10/2018, 02/11/2018, 17/11/2018, 22/12/2018, 27/12/2018, 01/01/2019, 20/02/2019, 17/03/2019, 11/04/2019, 05/06/2019, 05/07/2019, 13/09/2019, 28/09/2019, 03/10/2019, 23/10/2019, 28/10/2019, 02/11/2019, 07/11/2019, 17/11/2019, 22/11/2019, 02/12/2019, 07/12/2019, 12/12/2019, 04/07/2020

The accuracy was assessed using the root-mean-square error (RMSE), Equation (3), and mean percentage difference (MPD), Equation (4), considering the number of images utilized (n). The accuracy metrics were calculated by comparing the statistics of the water elevation intersections statistics (x_i) (Me, Mn, and Mo) with the observed water levels (x_o) (Table 5). Then the statistic with the best performance was used for the final analysis.

$$\mathrm{RMSE} = \sqrt{\frac{\sum_{i=1}^{n} (x_i - x_o)^2}{n}} \tag{3}$$

$$\mathrm{MPD}(\%) = \frac{\sum_{i=1}^{n} \left(\left| \frac{x_i - x_o}{x_o} \right| \cdot 100 \right)}{n} \tag{4}$$

Table 5. Observed water levels used to assess the accuracy.

No. of Datas	Date	Water Level [m]	Date	Water Level [m]	Date	Water Level [m]	Date	Water Level [m]
102	27/01/2017	414.65	20/10/2018	419.66	31/03/2019	420.08	07/11/2019	419.48
	10/02/2017	414.31	23/10/2018	419.64	11/04/2019	420.94	14/11/2019	419.41
	31/10/2017	412.59	26/10/2018	419.60	12/04/2019	420.94	16/11/2019	419.40
	20/11/2017	412.29	27/10/2018	419.60	25/04/2019	420.89	22/11/2019	419.34
	28/02/2018	418.11	02/11/2018	419.55	03/06/2019	420.61	02/12/2019	419.41
	24/03/2018	420.96	07/11/2018	419.49	05/06/2019	420.59	07/12/2019	419.37
	05/04/2018	420.93	17/11/2018	419.39	11/06/2019	420.55	08/12/2019	419.36
	17/04/2018	420.98	19/11/2018	419.37	23/06/2019	420.50	11/12/2019	419.33
	21/05/2018	420.78	01/12/2018	419.28	05/07/2019	420.44	11/12/2019	419.33
	28/06/2018	420.55	08/12/2018	419.23	17/07/2019	420.36	20/12/2019	419.24
	01/07/2018	420.53	13/12/2018	419.21	29/07/2019	420.29	27/12/2019	419.17
	09/07/2018	420.48	22/12/2018	419.24	10/08/2019	420.22	02/01/2020	419.22
	16/07/2018	420.44	24/12/2018	419.23	21/08/2019	420.15	13/01/2020	419.17
	19/07/2018	420.41	27/12/2018	419.21	22/08/2019	420.14	25/01/2020	419.11
	22/07/2018	420.39	31/12/2018	419.18	03/09/2019	420.05	06/02/2020	419.38
	30/07/2018	420.34	07/01/2019	419.11	13/09/2019	419.97	18/02/2020	419.34
	03/08/2018	420.31	18/01/2019	419.03	15/09/2019	419.96	12/05/2020	432.27
	04/08/2018	420.31	25/01/2019	418.97	27/09/2019	419.86	25/05/2020	432.27
	14/08/2018	420.24	30/01/2019	418.92	28/09/2019	419.85	05/06/2020	432.43
	15/08/2018	420.23	11/02/2019	418.83	03/10/2019	419.81	17/06/2020	432.43
	27/08/2018	420.13	20/02/2019	418.77	09/10/2019	419.75	29/06/2020	432.43
	08/09/2018	420.04	23/02/2019	418.74	21/10/2019	419.64	03/07/2020	432.42
	20/09/2018	419.94	07/03/2019	418.69	23/10/2019	419.63	11/07/2020	432.38
	23/09/2018	419.92	14/03/2019	418.62	24/10/2019	419.62	22/07/2020	432.34
	02/10/2018	419.83	17/03/2019	418.68	28/10/2019	419.58	-	-
	14/10/2018	419.72	19/03/2019	418.66	01/11/2019	419.54	-	-

A qualitative approach was also used to assess the water segmentation performance by comparing all the borderlines over Sentinel-2 RGB compositions and analyzing specific areas of the reservoir perimeter. This analysis made it possible to understand land interaction mechanisms and their respective effects on accuracy.

3. Results

3.1. SAR Data Thresholding and Environmental Influences on Backscattering

The number of water pixels in scenes from Sentinel-1A with VV polarization was higher than that obtained with VH polarization. Pixel densities showed a unimodal distribution (a small number of water pixels) and bimodal behavior (a higher amount of water pixels), respectively, for low and high reservoir storage levels (Figure 9).

Considering that one of the objectives of this study was to evaluate the operational feasibility of reservoir monitoring with SAR images and to investigate the environmental effects on segmentation, the thresholds were set through a graphical interpretation (a simplified method presented in Section 2.3).

The acceptable noise level, and hence the thresholding settings, become an arbitrary choice at some point, influencing variability patterns and results. To investigate this question, the thresholds obtained via the graph were compared to those obtained by intersecting SAR images with the contour line corresponding to the observed water level. In this process (similarly to the one detailed in Section 2.3), the SAR image is overlayed with the contour level derived by the DEM. Then, the mean VV and VH threshold values are extracted based on the geospatial intersection (similar process detailed in Section 2.3). In Figure 10, it can be observed that a similar pattern of the VV and VH thresholds was obtained for both methods.

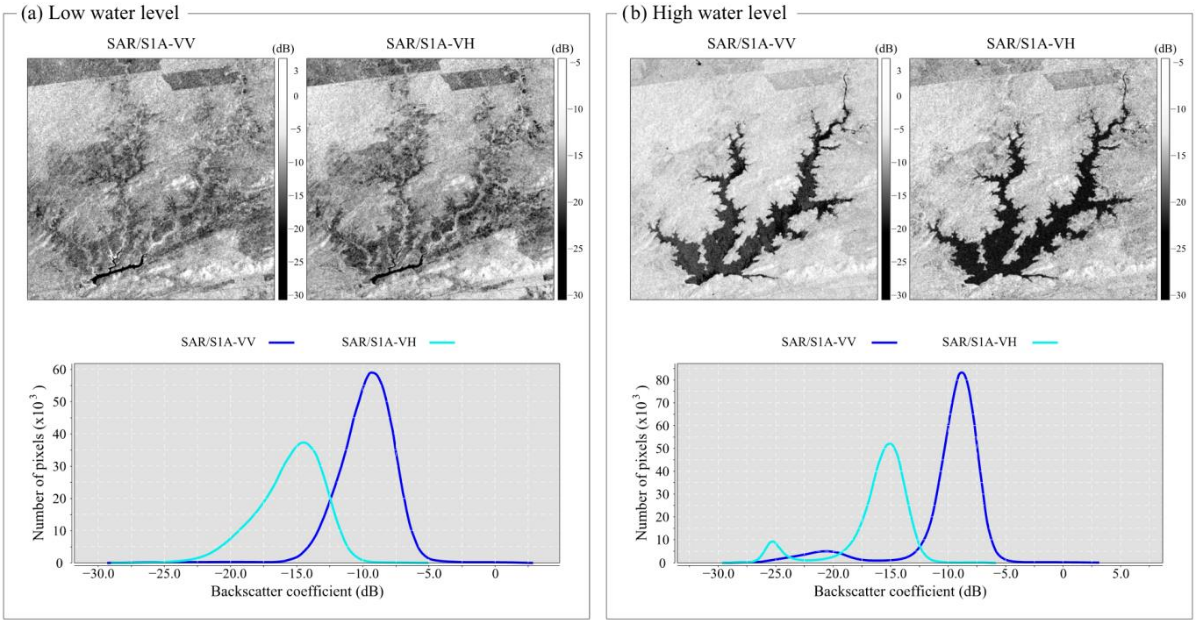

Figure 9. Sentinel-1A images: (**a**) low water level (16 February 2018) and (**b**) high water level (29 June 2020).

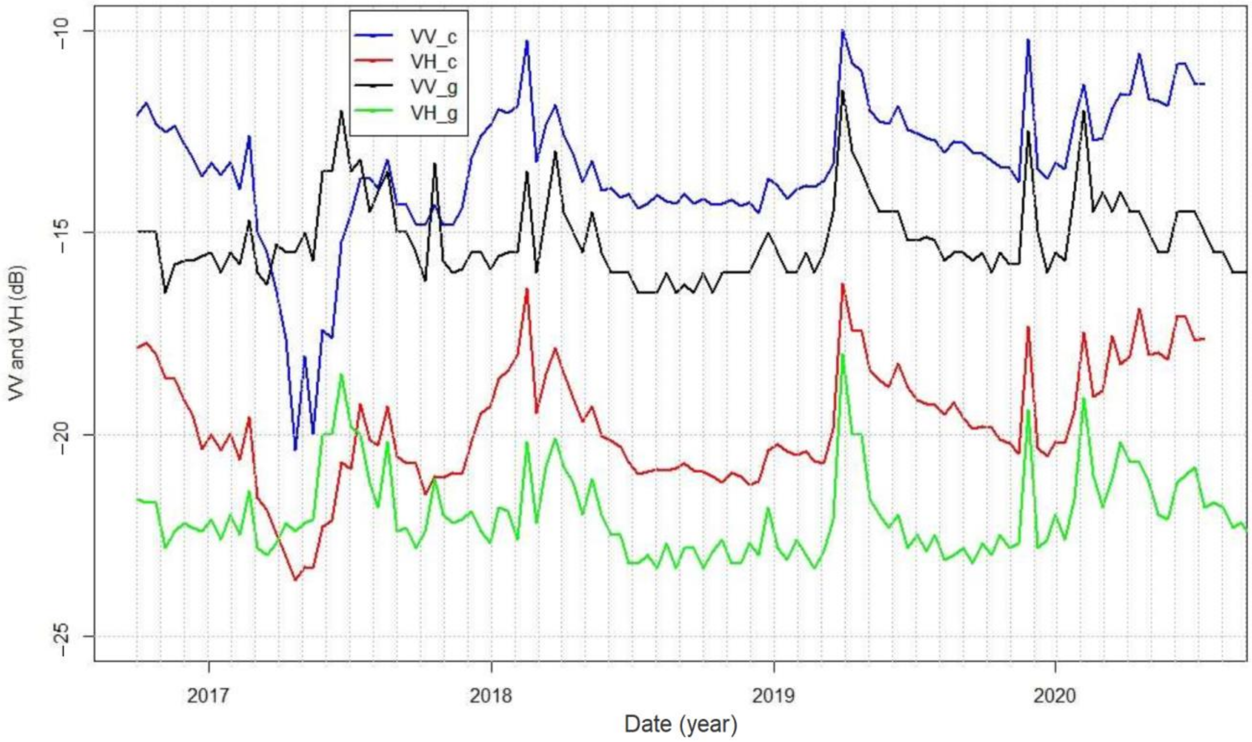

Figure 10. Comparison between VV and VH backscattering coefficient thresholds: (1) Calculated based on the intersection of the observed water elevation contour line over SAR images (blue and red lines: VV_c and VH_c) and (2) obtained via graphical interpretation (black and green lines: VV_g and VH_g).

The SAR backscattering threshold values obtained using the graphical method resulted in a mean value of −15.15 dB for VV, ranging from −16.5 to −11.5 dB, and a mean value of −21.97 dB for VH data, ranging from −23.3 to −18 dB (Table 6). Using the contour level method resulted in a mean value of −13.4 dB for VV data, ranging from −20.4 to −10.0 dB, and a mean value of −20.0 dB for VH data, ranging from −23.6 to −16.2 dB (Table 6).

Table 6. VV and VH threshold statistics: (1) obtained via graphical interpretation and (2) calculated based on the intersection of the observed water elevation contour line over SAR images.

Statistics	Graphical Method		Contour Level Method	
	VV	VH	VV	VH
Min.	−16.50	−23.30	−20.4	−23.6
1st Quartile	−15.97	−22.70	−14.2	−20.7
Median	−15.50	−22.20	−13.4	−20.0
Mean	−15.15	−21.97	−13.4	−20.0
3rd Quartile	−14.50	−21.60	−12.3	−18.6
Max.	−11.50	−18.00	−10.0	−16.2
(max–min)	5.00	5.30	10.4	7.4

Seasonal patterns in SAR backscattering threshold variations are shown in Figure 11. The lower level usually occurred in the dry season and the higher level in the wet season. This pattern was the same for VV and VH polarization, NDVI, and 30 day accumulated precipitation (Pac30). All signals in Figure 11 seem to be coherent in time.

The CWT wavelet power spectrum analysis (Figure 12) showed that for precipitation (Figure 12a), the power of variance was concentrated in the wet seasons, localized in 2018, 2019, and 2020, ranging from a 10 to an 80 day band. The NDVI power spectrum (Figure 12b) was more significant at the year scale (~320 day band), and during all positions, significant peaks were noted in 2017 (40 day) and 2020 (10–40 day band) at higher frequencies. However, it can be observed that variance was very low down to the 40 day band, except for 2020. A strongly significant peak was identified from the end of 2018 to May 2019, at the 80–100 day band, indicating an intraseasonal variance. The annual signal (frequencies lower than ~320 day band) was also stronger (dark red) in these years. The soil moisture (SSM) power spectrum (Figure 12c) showed significant variance at higher- and lower-scale frequencies (down to the 40 day band) during almost all wet seasons, except for 2017.

WTC then was applied to identify causality relationships by analyzing variable time series together in the time-frequency space. The WTC between the normalized difference vegetation index NDVI and VV and VH (Figure 13c,d) showed a well-defined significant common power in the 80–120 day band between May 2018 and August 2019.

The WTC between surface soil moisture (SSM) and VV (Figure 13e) presented some common power peaks at different higher frequencies, above the 80 day period. A strong signal was observed at the 30–60 day band of the wet season of 2018, but the phase arrows pointed down, which means the VV was leading SSM. However, this makes no physical sense since the SSM does not depend on VV; hence, this result will not be considered in our analysis. On the seasonal scale, there was a significant peak between 2018 and 2019, but the phase was not defined.

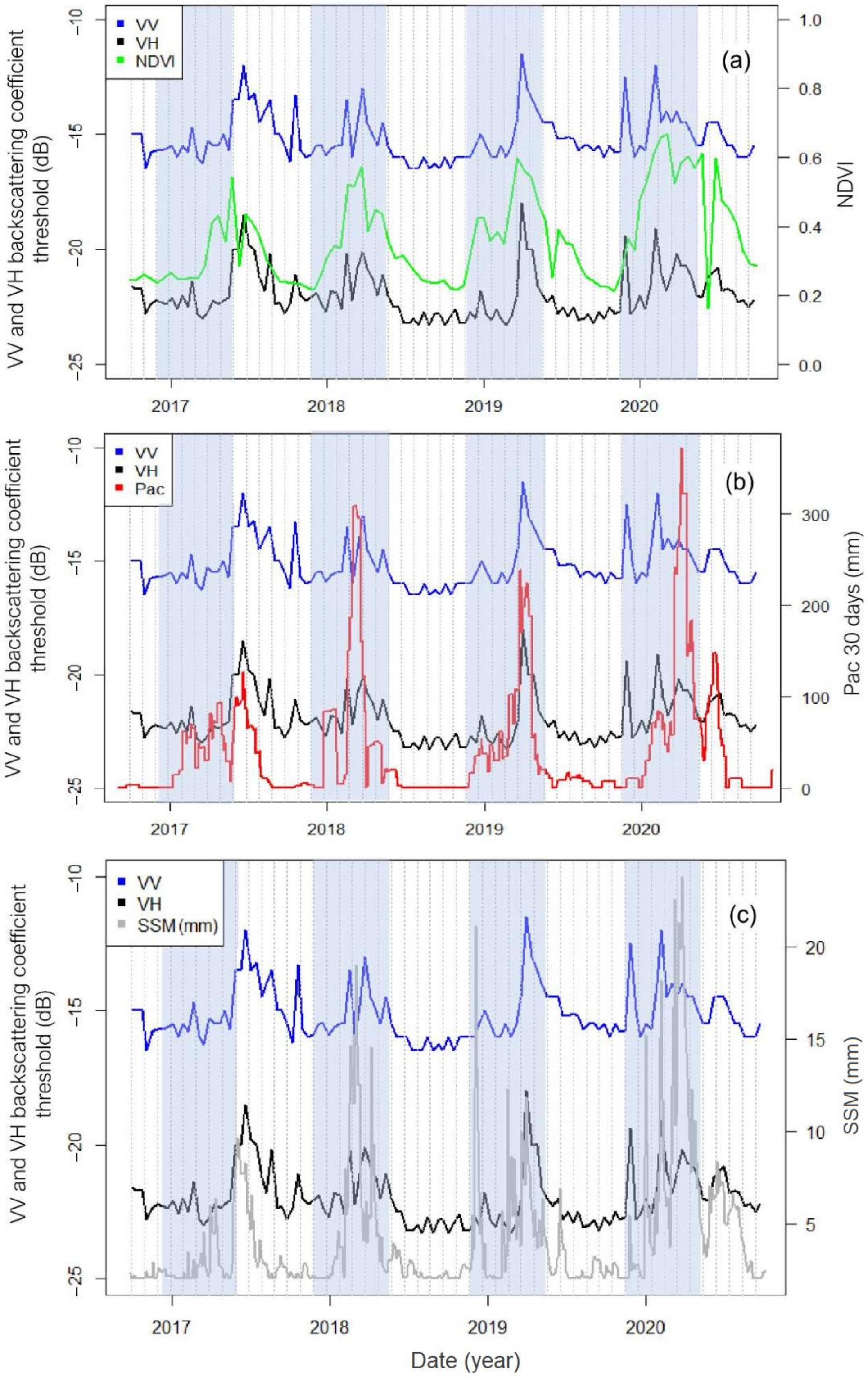

Figure 11. Comparison between VV and VH backscattering coefficient thresholds, NDVI signal (**a**), 30 day accumulated precipitation (Pac30) (**b**), and surface soil moisture (SSM) (**c**). Shaded areas indicate the months corresponding to the wet season.

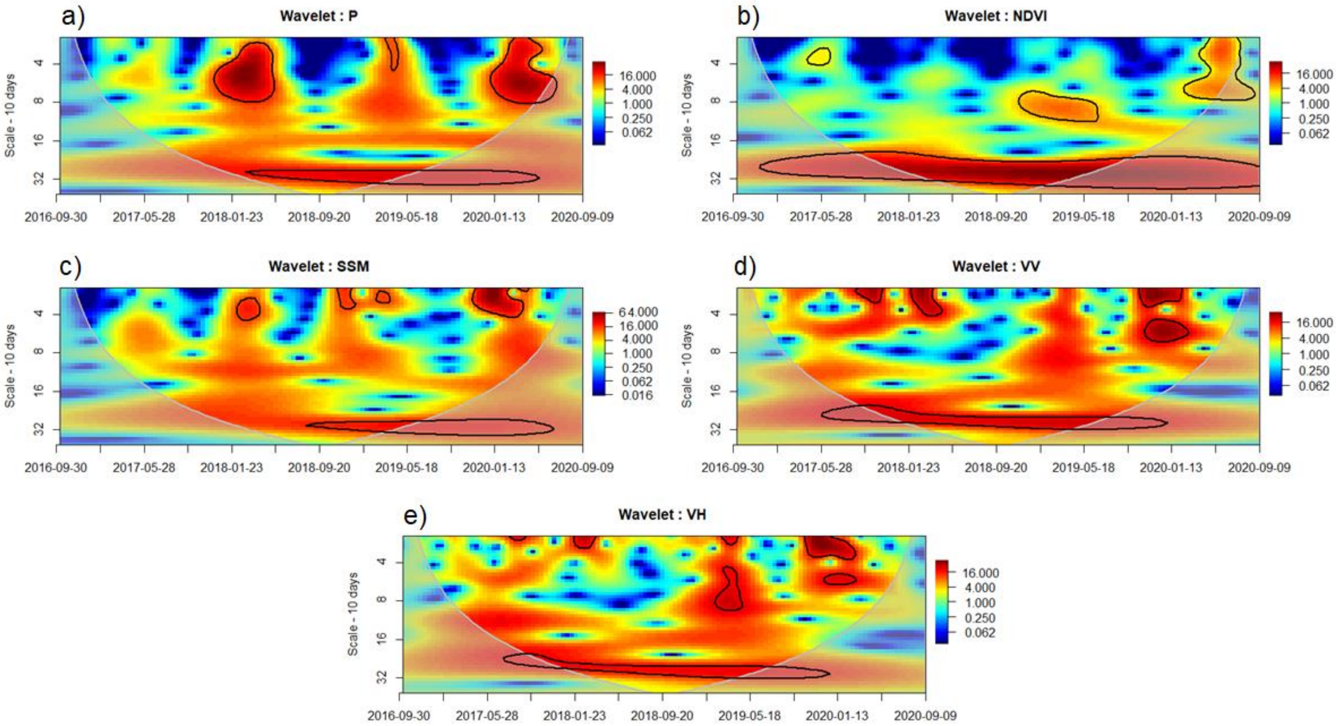

Figure 12. Continuous wavelet transformation (CWT): (**a**) daily precipitation (P); (**b**) normalized difference vegetation index (NDVI); (**c**) surface soil moisture (SSM); (**d**) VV polarization; (**e**) VH polarization. Notes: time is displayed on the horizontal axis, frequency on the vertical axis; warmer colors (red) represent high power signals, and colder colors (blue) represent low power; power scale bars are shown to the right of the charts; the thick contour indicates the 95% significance level against white noise; the cone of influence (COI) is shaded.

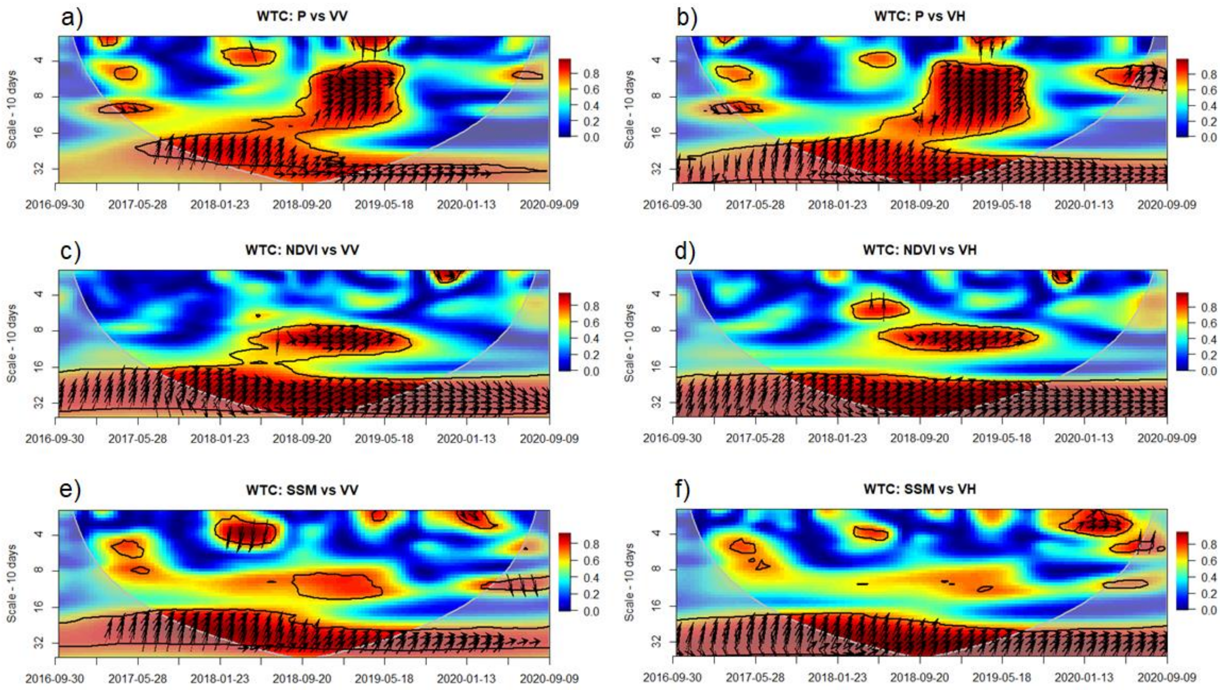

Figure 13. Wavelet transform coherence (WTC) between (**a**) P and VV, (**b**) P and VH, (**c**) NDVI and VV, (**d**) NDVI and VH, (**e**) SSM and VV, and (**f**) SSM and VH. Notes: time is displayed on the horizontal

axis, frequency on the vertical axis; warmer colors (red) represent high power signals, and colder colors (blue) represent low power; power scale bars are shown to the right of the charts; the thick contour indicates the 95% significance level against white noise; the cone of influence (COI) is shaded.

Figure 14 illustrates the linear correlation matrix between environmental variables P, SSM, NDVI, and VV/VH polarizations. Although VV was more correlated with the 32 day average NDVI (NDVI.32) and VH was more correlated with the 30 day average soil moisture (SSM.30), it can be observed that all correlations between accumulated precipitation (P.30, P.22) and other temporal scales of averaged NDVI/SSM with VV/VH were significant ($p < 0.001$).

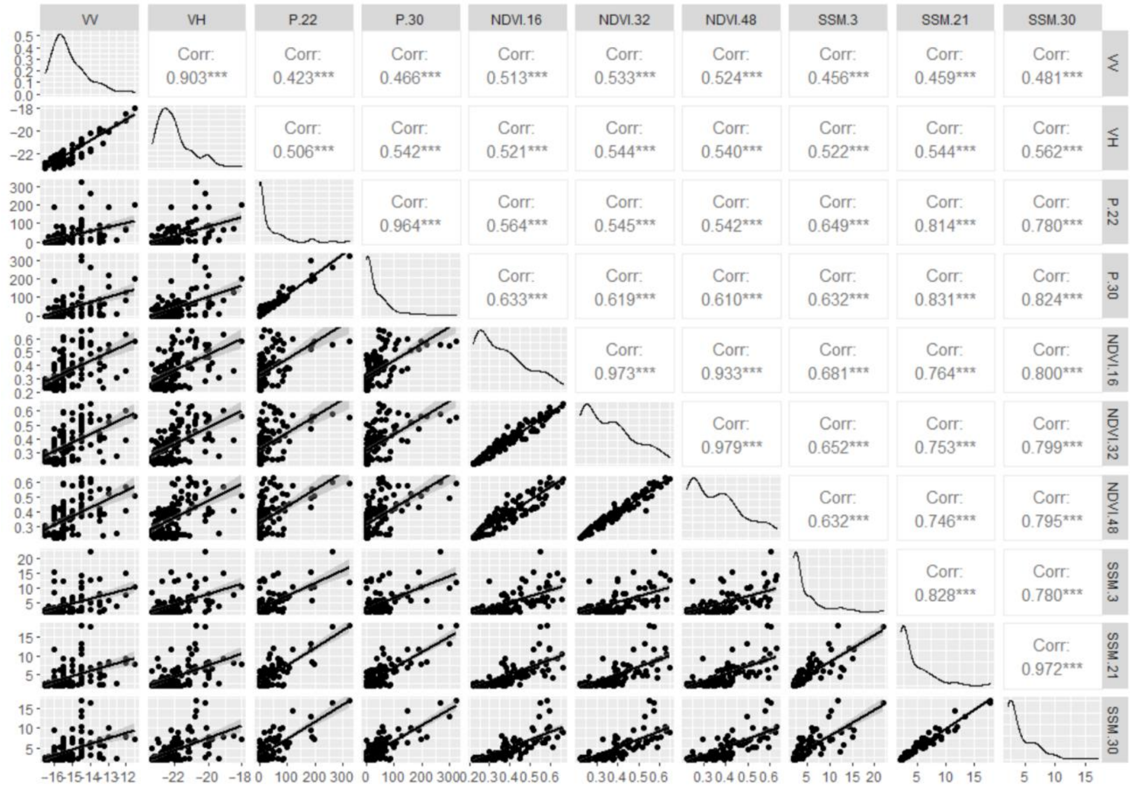

Figure 14. The correlation matrix of environmental variables, VV, and VH polarizations. Notes: charts on the matrix diagonal represent density distributions of values; charts on the top-right show linear correlation, characters "***" represent the significance of correlation at $p < 0.001$; charts on the bottom-left side present graphical scatter plots and linear regression models.

3.2. Accuracy Assessment

3.2.1. Statistics

Once the water level retrieving process was completed, based on the intersection between the water feature outlines and DEM, generating the mean (Me), median (Mn), and mode (Mo) for each estimate, their influences on accuracy were investigated. The dates of the images in Tables 3 and 5 were tested in this investigation. For each image group (index) three water levels (WL (Me), WL (Mn), and WL (Mo)) were tested. Table 7 illustrates that the best results for all products (lower RMSE and MPD values) were obtained by employing the mode statistic (Mo) in retrieving the water level.

Table 7. RMSE and MPD results in the assessment of hydrological monitoring.

Product	**No of Images**	**WL (Me)**		**WL (Mn)**		**WL (Mo)**	
		RMSE (m)	**MPD (%)**	**RMSE (m)**	**MPD (%)**	**RMSE (m)**	**MPD (%)**
NDWI/L8	12	1.01	0.23	1.01	0.23	0.89	0.20
MNDWI/L8		0.66	0.14	0.67	0.15	0.55	0.12
NDWI/S2	32	0.74	0.17	0.61	0.14	0.44	0.10
MNDWI/S2		1.03	0.24	0.87	0.21	0.58	0.13
SAR/S1A-VV	61	1.32	0.29	1.16	0.25	0.87	0.19
SAR/S1A-VH		1.88	0.42	1.56	0.35	1.15	0.24

Note: WL is the water level.

3.2.2. Water Level and Storage Effects

The water level time series were retrieved and compared to the observed data, covering a period of 3.5 years, from 27 January 2017 to 22 July 2020. As mode (Mo) performed the best for both optical and SAR observations (Table 7), this statistic was employed to retrieve remote sensing water levels (Figure 15).

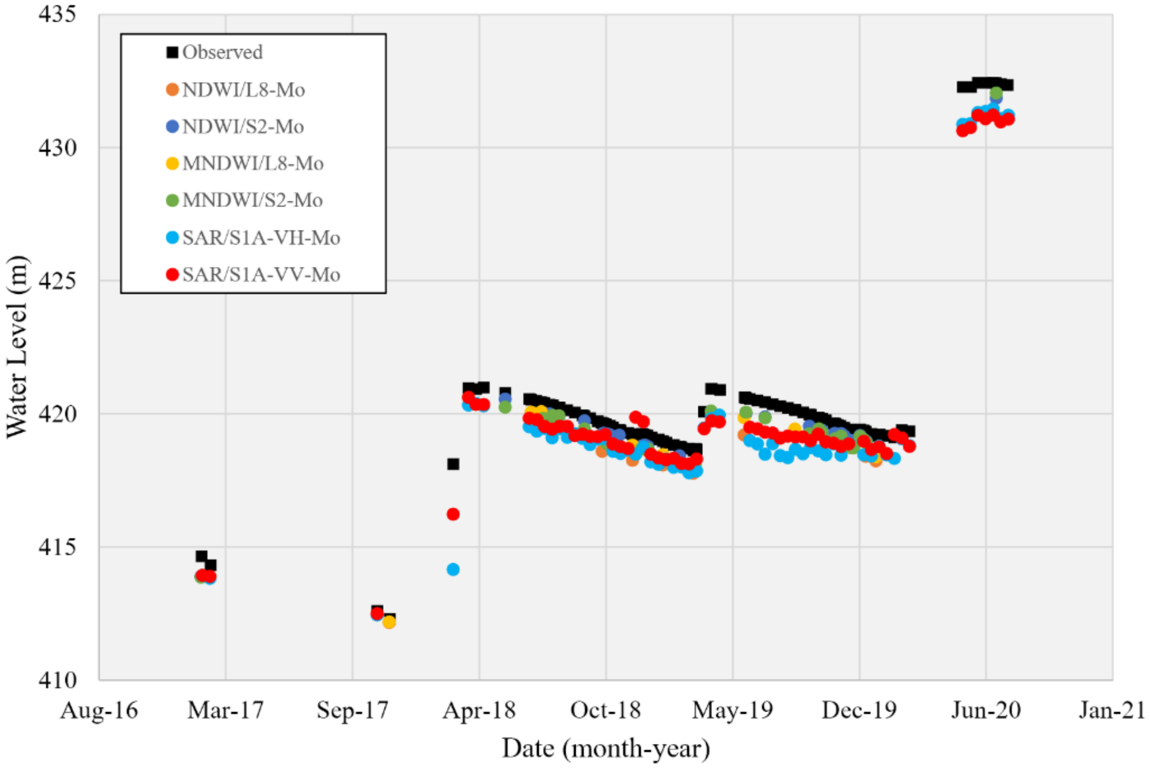

Figure 15. Comparison between reconstructed and observed time series water levels using remote sensing.

Figure 15 also illustrates that the estimated water levels were closer to observations when the water levels were lower than 420 m. The results were worse at storage levels higher than 420 m.

Table 8 presents a comparative analysis of water level accuracy between SAR and multispectral observations. With the aim of investigating the effects of storage levels on the accuracy, their metrics were stratified considering an arbitrary water level threshold of 420 m, chosen by analyzing Figure 15. The results indicate that RMSE and MPD were marginally higher when the water level was <420 m, and the percentile of errors higher than 1 m increased when the water level was >420 m.

Table 8. Accuracy of water level monitoring.

Water Level < 420 m						
Product	**<1 m (%)**	**RMSE (m)**	**MPD (%)**	**≥1 m (%)**	**RMSE (m)**	**MPD (%)**
NDWI/L8	83	0.79	0.18	17	1.25	0.30
MNDWI/L8	100	0.58	0.13	-	-	-
NDWI/S2	100	0.43	0.10	-	-	-
MNDWI/S2	100	0.58	0.13	-	-	-
SAR/S1A-VV	80	0.64	0.15	20	1.22	0.28
SAR/S1A-VH	65	0.67	0.17	35	1.68	0.37
Water Level ≥ 420 m						
Product	**<1 m (%)**	**RMSE (m)**	**MPD (%)**	**≥1 m (%)**	**RMSE (m)**	**MPD (%)**
NDWI/L8	-	-	-	-	-	-
MNDWI/L8	100	0.42	0.10	-	-	-
NDWI/S2	100	0.46	0.10	-	-	-
MNDWI/S2	100	0.60	0.14	-	-	-
SAR/S1A-VV	30	0.54	0.12	70	1.39	0.32
SAR/S1A-VH	40	0.73	0.17	60	1.24	0.29

Note: the symbol (-) means no data.

3.2.3. General Accuracy of Optical and SAR Water Data

Figures 16 and 17 can be used to evaluate the capacity of all products to delineate the reservoir surface water. The scenes were selected in the dry season. Figure 16 represents a situation in which the reservoir is empty, and in Figure 17, the reservoir storage is full. For both situations, the water borderline was extracted considering NDWI/L8, MNDWI/L8, NDWI/S2, MNDWI/S2, SAR/S1A-VH, and SAR/S1A-VV. These polygons were then compared to the water contour level derived from DEM, corresponding to the observed/interpolated water level.

Figures 16a–c and 17a–c illustrate typical features of the depletion zone: rocks, caatinga vegetation, bare soil, and typical eutrophication. In inlet branches, in the presence of eutrophication (Figure 17f), both SAR/S1A-VV and SAR/S1A-VH led to omission errors when compared to water extraction from optical images. Omission errors were also noted in delimitations using MNDWI/S2 and NDWI/S2 (Figure 17e), and were not present in Figure 16e,f when the storage levels were lower.

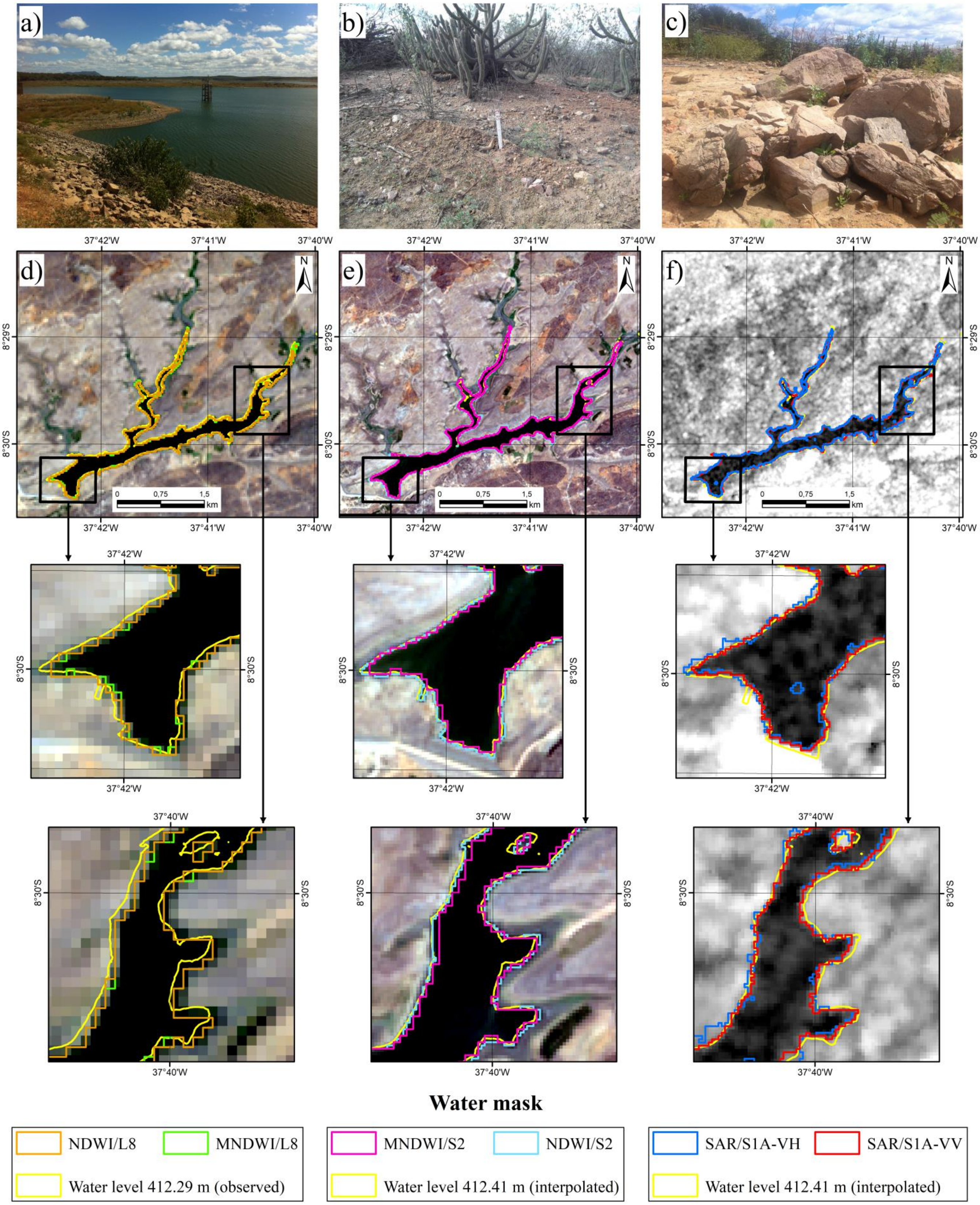

Figure 16. Water delimitation comparison with a low water level: (**a**) reservoir, (**b**) vegetation, (**c**) rock, (**d**) Landsat-8 (19 November 2017), (**e**) Sentinel-2 (12 November 2017), and (**f**) Sentinel-1A (12 November 2017).

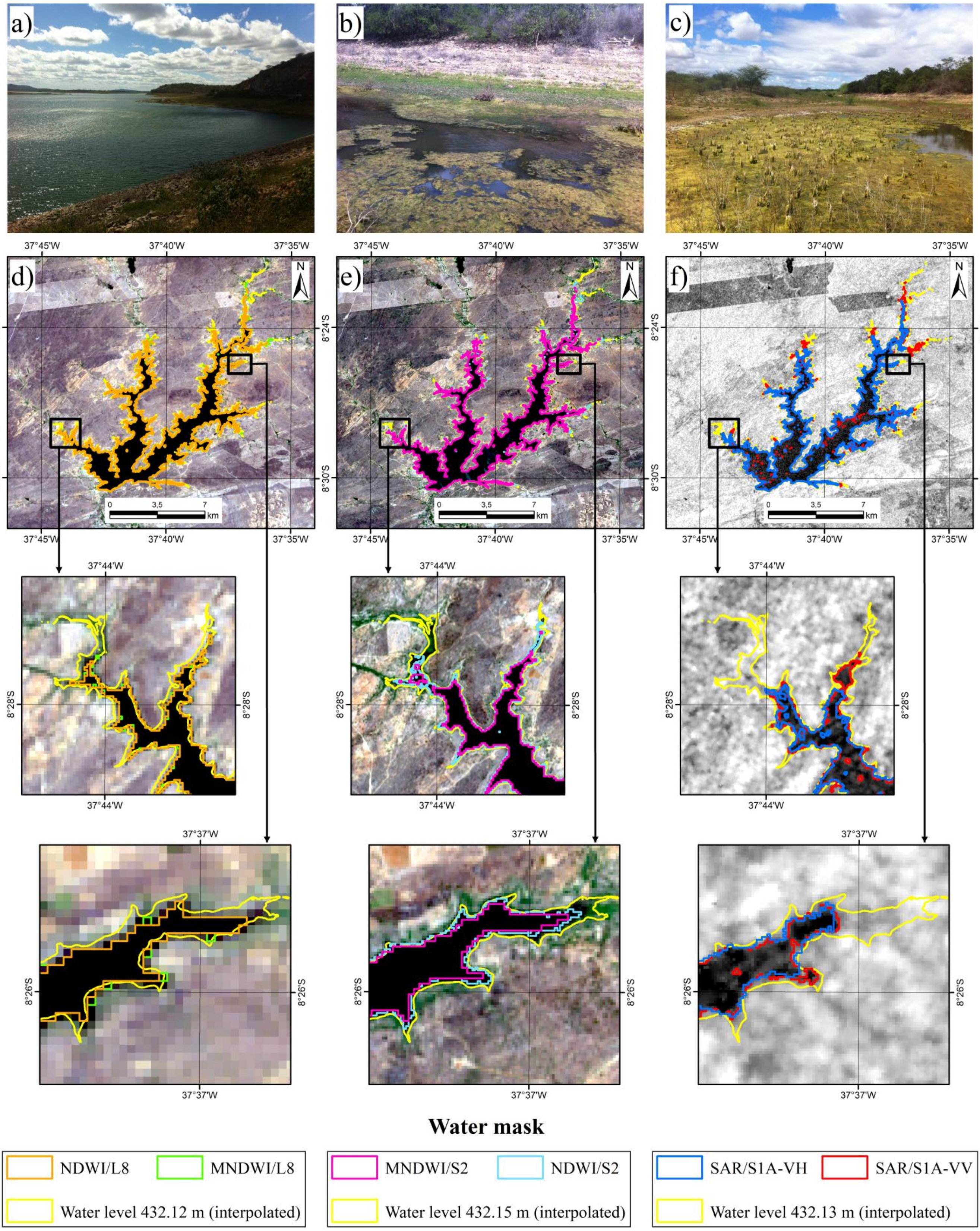

Figure 17. Water delimitation with a high water level: (**a**) reservoir, (**b**) eutrophication, and (**c**) typical eutrophicated inlet branch, (**d**) Landsat-8 (24 September 2020), (**e**) Sentinel-2 (17 September 2020), and (**f**) Sentinel-1A (21 September 2020).

4. Discussion

4.1. SAR Data Thresholding and Environmental Influences on Backscattering

Comparing the VV and VH threshold statistics in Table 6 to the average backscatter (dB) values for different water features found by Manjusree et al. [27], the SAR VV thresholds were similar to those of partially submerged water (−18.0 to −8.0 dB), whereas VH thresholds were similar to those of lake features (−32.0 to −21.0 dB) or flood water (−24.0 to −15.0 dB). It should be noted that the values in Table 6 refer to thresholds, whereas the values in Manjusree et al. [27] refer to average pixel values over water bodies. Our VV values also intersect the range of −25 to −15 dB for water center clusters found by Gulácsi and Kovács [26] and were strongly similar to the values of VH (−21.61 to −25.05 dB) and VV (−11.97 to −16.73 dB) for bare soil measured by Ezzahar et al. [33]. Considering that the borderline of the lake is on the limit between water and non-water features, the range of backscatter values obtained in this study is within the expected range, based on the aforementioned previous results.

The time variation patterns of the VV and VH backscattering coefficient thresholds illustrated in Figure 10 indicate that using a single threshold may not be appropriate for delineating water from non-water features during all seasons. Operational monitoring requires knowledge of the main factors that affect the backscattering and, consequently, water segmentation accuracy.

All signals (P, SSM, NDVI, VV, and VH) shown in Figure 11 seemed to be coherent in time. Precipitation is the atmospheric force that implies soil moisture (SSM) and vegetation vigor (NDVI) changes, but both can affect backscattering together or in isolation. VV polarization is mainly sensitive to surface roughness (soil, upper canopy), and VH is more responsive to volumetric scattering and is positively related to the amount of biomass [34]. Furthermore, meteorological events can bring about changes in the dielectric properties of features [33].

Comparing VV and VH backscattering and NDVI images regarding a typical depletion zone feature during the dry (Figure 18) and wet seasons (Figure 19), it can be noted that roughness was enhanced during the wet season. However, there was no significant visual pixel-level coherence between NDVI and backscattering VV and VH, suggesting that surface soil moisture plays a more substantial role in backscattering increasing even when NDVI is not high. Furthermore, Figures 18 and 19 illustrate that VH polarization showed less contrast between water and non-water features, even during the wet season when high-NDVI pixels were detected.

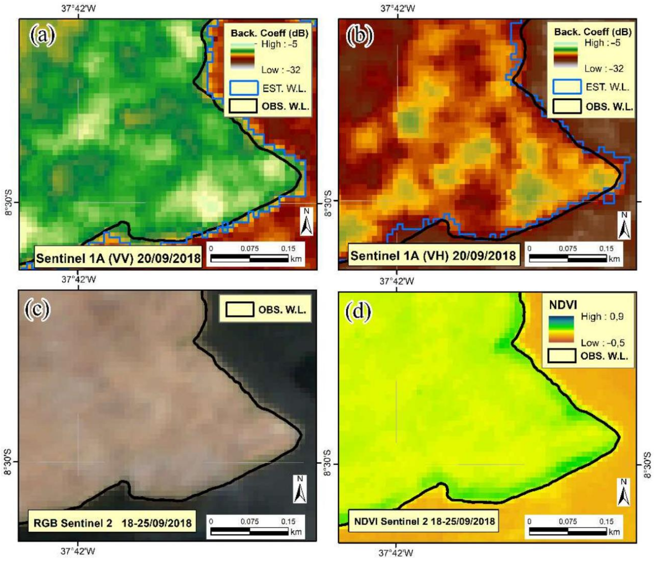

Figure 18. Typical depletion zone image features in the dry season: (**a**) VV backscattering; (**b**) VH backscattering; (**c**) RGB composition; and (**d**) NDVI composite. OBS. W.L indicates observed water level.

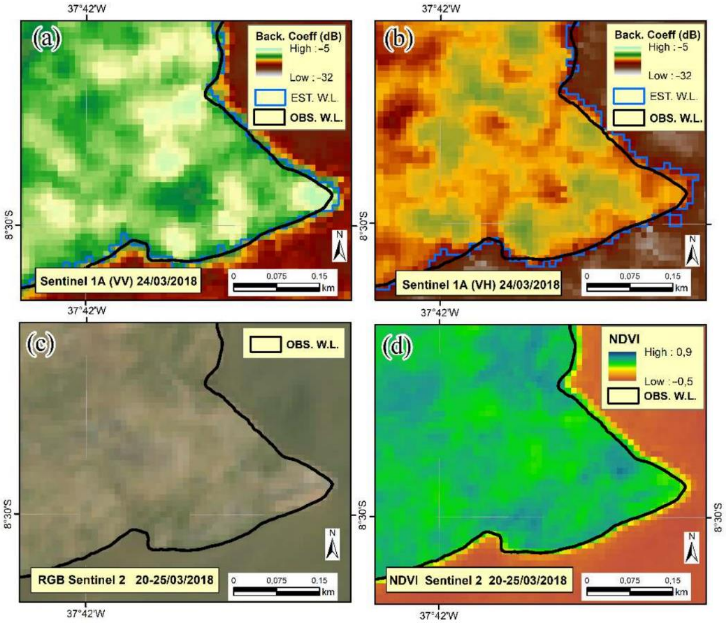

Figure 19. Typical depletion zone image features in the rainy season: (**a**) VV polarization backscattering; (**b**) VH polarization backscattering; (**c**) RGB composition; and (**d**) NDVI composite. OBS. W.L indicates observed water level.

The CWT analysis (Figure 12) showed that, as expected, P and SSM presented similar structures at higher and lower frequencies. Despite the evapotranspiration and runoff, the spatial and temporal patterns of soil moisture depend on the precipitation variability [55]. The same can be noted for VV. The significant peaks were in the middle of 2017 and in the wet seasons of 2018 and 2020. For the VV and VH spectra, the same pattern was identified except that in 2019 there was also a significant power (Figure 12d,e, respectively). The annual signal for VV and VH was also significant.

The WTC between daily precipitation (P) and VV (Figure 13a) showed a significant common power between May 2018 and September 2019 at the 60–120 day band, which could be used to characterize a strong seasonal signal during these years. In this strong common power signal, the phase arrows were pointing to the right, which means that the series were in phase. At lower frequencies, below the 160 day period, the significant common power area showed the phase arrows pointing to the right and up, which meant that the second variable was leading. However, this makes no physical sense in this case, once the precipitation is not dependent on VV, and VH showed a significantly high correlation in some specific periods (Figure 13a,b). The coherence between P and VH (Figure 13b) shows the same pattern of common power structures as the previous analysis. Except for the peak at the 60–120 day band, the phase arrows pointed to the right and up, which means that P was leading VH.

The WTC between NDVI and VV and VH (Figure 13c,d) showed that NDVI was in phase with VV and led VH at the significant common power at the 80–120 day band, between May 2018 and August 2019. The annual signal showed a strong common power with phase arrows pointing to the right and up, meaning that NDVI was leading the VV and VH signals. NDVI was more correlated to VV and VH near the year-band and was found to have a high correlation in two isolated areas around 80 days and the 10–20 day band. SSM showed significant correlation areas in all bands, although not continuously.

The annual signal was significant, with phase arrows pointing to the right and up, which can be understood as indicating that the SSM was leading the VV signal (Figure 13e). The common power between SSM and VH (Figure 13f) showed an isolated signal at higher frequencies in the wet season of 2020 and the series were in phase. The annual signal presented the same structure and phase found in the SSM and VV relationship.

The main causal relationship between SSM, VV, and VH series was observed at the annual signal and always showed that the first variable was leading the second one. Isolated responses at higher frequencies were predominantly observed in the wet seasons. Differences between the years at these frequencies could have occurred due to year-to-year variability. However, to detect anomalies, it would be necessary to analyze long-term time series to relate them to climate signals.

The results show that soil moisture variations supplied by precipitation controlled the SAR backscattering polarization in our study area. Although scattering contributions from soil moisture variations are drastically smaller than surface roughness [37,56], they controlled the signal responses. This means that the bare soil feature, the most predominant land-use characteristic present in the depletion zone, controlled the backscattering threshold variability.

Although the use of wavelets was a helpful tool in understanding the time-frequency relationship between variables, it was not an easy-to-use tool to predict VV and VH backscatter changes by itself. If one is interested in operational SAR applications, NDVI or precipitation (P) can be used as a predictor variable. The linear correlation matrix presented in Figure 14 showed that despite the physical changes in VV and VH backscattering caused by soil moisture, VV was more correlated with the 32 day average NDVI (NDVI.32), and VH was more correlated with the 30 day average soil moisture (SSM.30). Figure 13 also shows that NDVI was strongly correlated to precipitation and soil moisture variations, as expected based on the literature.

The highest VV/SSM correlation was 0.481 and that of VH/SSM was 0.562 (Figure 14). The correlations found by Ezzahar et al. [33] using measured soil moisture were 0.84 for VV/SSM, and 0.61 for VH/SSM. The vegetation index has already been employed in correction algorithms to estimate soil moisture in passive microwave remote sensing, improving its correlation drastically [57]. Considering that in this study we employed a 10 km SSM image resolution, VV and VH prediction could be drastically improved by choosing better predictors, preferentially with higher-resolution products, or using more robust techniques, such as machine learning models. It could be useful to set thresholds in automatic extraction applications.

Regarding the setting of thresholds, our results are in agreement with those of Altese et al. [39], who achieved an important finding related to the sensitivity of the backscatter coefficient to the dielectric constant. According to the authors, a range of variation of 5 dB was always observed from dry to wet conditions, regardless of the surface soil roughness and radar configuration. The amplitude in threshold variations found in our experiment (Table 6) and the range in threshold variations illustrated in Figure 11 corroborate this important finding, supported by theoretical scattering modeling.

Therefore, our results indicated that threshold adjustments according to soil moisture states in dry or wet conditions can be carried out more straightforwardly, as long as they are in the presence of bare soil water features, such as a reservoir depletion zone. Influences due to soil types on backscattering have also been mentioned in the literature. Leween et al. [58] noticed that in the presence of sandy soils, the backscatter was lower, resulting in the overestimation of water pixels, which in their study required an empirical thresholding calibration step, in which they reduced the upper threshold by 25%. The authors also mentioned the need to investigate backscattering in sandy soils in future works.

4.2. Accuracy Assessment

According to Table 7, the best RMSE (Equation (3)) and MPD (Equation (4)) results were obtained using the mode and median in the second position. These results follow the findings of Weekley and Li [59], who argued that the mean and the median are most susceptible to outlier influences, whereas the mode statistic assesses the central tendency of the value within the boundary. One crucial fact is that the best accuracy of the mode statistic was maintained when using a better resolution (as employed in this study) compared to the 30 m resolution used by Weekley and Li [59] (Landsat-5 and Shuttle Radar Topography Mission DEM).

Observing Figure 15, it can be noted that the estimated water elevations were closer to the observed data when the water levels were lower than 420 m. The results were worse at storage levels higher than 420 m. Although accuracy was slightly higher when the water level was higher than 420 m (lower RMSE and MPD values) (Table 8), the percentile of errors less than 1 m were drastically decreased from 80% to 30% for Sentinel-1A-VV and 65% to 40% for Sentinel-1A-VH. Sentinel-2 and Landsat-8 percentile errors appeared not to be affected by water level storage. According to Özelkan [60], who noted that when lake area increases, interactions between the lake boundary and land cover classes affect water mapping performance, poor performance using Landsat-8 data was expected when water elevations were higher.

Analyzing Table 8 and Figures 16 and 17, the results provide evidence that interactions with land use on the border with water bodies affected SAR performance more negatively than the optical scenes, especially in the reservoir inlet branches—regions where optical complexity increased as reservoir storage levels increased. In these areas, with the presence of caatinga, bare soil, and aquatic macrophytes caused by eutrophication, SAR images did not perform well. Conversely, the MNDWI/S2 and NDWI/S2 indices performed better due to their ability to maximize the reflectance of the water in the visible region and to minimize its effect in the infrared spectra, which, combined with the better spatial resolution of this sensor, resulted in enhanced performance. The water detection mechanism with SAR images is based on the contrast between the backscatter signal intensity between liquid surfaces, land, and vegetation.

In our study, omission errors using SAR images were more frequent, especially in the reservoir inlet branches (Figure 17b,c,e,f), which occurred when the reservoir storage level was high. In our case, the surface vegetation was high enough to influence the signal backscatter and, despite the presence of chlorophyll in the water, the results of the multispectral images were better. The same did not occur in a study by Bolanos et al. [61], in which the effect of chlorophyll on reflectance in optical images was greater than the effects of vegetation on backscatter, leading to false positives in SAR images. Our results are in accordance with those of Gulácsi and Kovács [26], who found that in wetlands, the water cover under the vegetation canopy is not detected with SAR, and the area calculated using the MNDWI spectral index is generally higher than the area calculated based on SAR. Therefore, we also deduce that the type and stage of vegetation can significantly influence the results of SAR images.

Compared to optical images, the performance of Sentinel-1A-VV data was similar to that of NDWI/Landsat-8 and lower than MNDWI/Landsat-8, MNDWI/Sentinel-2, and NDWI/Sentinel-2 products. Considering the results, NDWI/Sentinel-2 showed the best performance due to its spatial resolution of 10 m, compared to the MNDWI/Sentinel-2 resolution of 20 m. Nevertheless, a systematic error (not investigated in this work) was evident in Figure 15, and after a bias correction, the RMSE values related to mode statistics were drastically reduced (results not shown in Table 7), as follows: MNDWI/Sentinel-2 (0.15 m), NDWI/Sentinel-2 (0.16 m), MNDWI/Landsat-8 (0.19 m), NDWI/Landsat-8 (0.31 m), SAR/1A-VV (0.44 m), and SAR/S1A-VH (0.54 m). This systematic error may have originated due to the edge effects of pixels that occurred during intersection operations, and further investigations, such as those conducted by Weekley and Li [59], who tested three types of boundaries, may contribute to this bias removal process in future research. Even after bias correction, optical imagery outperformed SAR data, and despite the coarse resolution, MNDWI/Sentinel 2 slightly outperformed NDWI/Sentinel 2.

One potential caveat is that multispectral image performance may be drastically enhanced by adjusting thresholds for each optical scene instead of using the default zero. Thresholds vary depending on the location, collection, image correction level [3], and sensor type. However, considering the experiments carried out by Reis et al. [62] in the same study area investigating uncertainties associated with optimized thresholds, the accuracy results using default zero thresholds can be considered satisfactory for the purpose of comparison.

The graphical approach employed in threshold determination, presented in Section 2.3, led to biased results, as illustrated in Figure 10. A bias of -1.75 dB was identified for the mean values of VV polarization and -1.97 dB for VH, which is explained by excusing the visual presence of disconnected water pixels not only outside the reservoir (commission errors) but also the omission errors inside the reservoir water body, the latter being caused by the presence of wind speeds above the Bragg resonance threshold, shown in Figure 3 and Section 2.2.1. We did not assess the impact of bias correction on the accuracy, but a gain is expected.

5. Conclusions

SAR and multispectral data can be successfully combined for use in reservoir monitoring. Hydrological variables, such as the water level of stored water can be derived from the combined analysis of these satellite data. In particular, the performance of Sentinel-1, Landsat-8, and Sentinel-2 data in terms of data availability, polarization performance, accuracy, and surrounding environmental influences were assessed in this work to monitor the Poço da Cruz reservoir, located in a semi-arid region in northeast Brazil. According to our results, SAR imagery is suitable for operational reservoir monitoring, especially when optical images or ground truth data are unavailable. We were able to conclude that:

- The use of SAR Sentinel-1 imagery allowed for the monitoring of reservoir water levels in an uninterrupted manner, with no gaps, whereas the low availability of optical images that were free from atmospheric interference proved to be unfeasible for operational monitoring.
- According to the methodology employed in water/non-water segmentation, VV polarization outperformed VH polarization. VV and VH reference water values depended on their position in the water body. Pixels on the water/non-water edge may represent values typical of soil features.
- During wet seasons, the contrast between water/non-water features was enhanced, and thresholds must be set according to soil moisture, as soil characteristics related to water absorption and changes in dielectric properties influence backscatter.
- NDVI and 30 day accumulated precipitation can be used to predict VV and VH thresholds, as well as machine learning models or more sophisticated algorithms with the aim of automating water segmentation.
- In the presence of a bare soil reservoir depletion zone, simple empirical threshold adjustments of about 5 dB can also be set to improve water extraction in the changes of dry to wet conditions.
- Compared to satellite optical images, the accuracy of SAR was equivalent to that of NDWI/Landsat-8.
- Optical image accuracy outperformed SAR image accuracy in inlet branches, where the complexity of water features was higher due to the diversity of features and the presence of aquatic macrophytes. Land use interactions can affect SAR data more negatively than multispectral images.
- Mode statistics showed to be the most appropriate for retrieving water levels when applying this methodology.
- Even employing the visual water extraction approach, SAR imagery proved to be suitable for operational monitoring not only when optical images are unavailable due to weather conditions but in order to maximize accuracy in situations when SAR data cannot perform well.
- The graphical approach to the selection of SAR backscattering thresholds led to biased results that underestimated the number of water pixels. A bias correction step must be added, with the aim of achieving better results. One of the advantages of the graphical approach is to maximize the number of SAR images, enabling one to use data obtained under unfavorable wind stress conditions.

Author Contributions: Conceptualization, W.d.O.S., L.G.d.M.R. and A.R.N.; data curation, W.d.O.S., L.G.d.M.R. and A.R.N.; formal analysis, W.d.O.S., L.G.d.M.R., D.V. and A.R.N.; investigation, W.d.O.S., L.G.d.M.R., D.V. and A.R.N.; methodology, W.d.O.S., L.G.d.M.R., D.V. and A.R.N.; supervision, C.R.F.J., A.R.N., A.M.R.-A., J.J.d.S.P.C. and S.M.G.L.M.; validation, W.d.O.S., L.G.d.M.R., A.M.R.-A., D.V., A.R.N., C.R.F.J., J.J.d.S.P.C. and S.M.G.L.M.; writing—original draft, W.d.O.S., L.G.d.M.R., C.R.F.J. and A.R.N.; writing—review and editing, A.M.R.-A., J.J.d.S.P.C. and S.M.G.L.M. All authors have read and agreed to the published version of the manuscript.

Funding: This research received no external funding.

Acknowledgments: The authors would like to thank the Brazilian National Water Agency (ANA) and the Pernambuco Water and Climate Agency (APAC) for making data available. D.V., A.R.N., J.J.d.S.P.C. and S.M.G.L.M. thank to CNPq Productivity in research (PQ). Research was supported by POAIUJA 2021-22 and CEACTEMA from the University of Jaén (Spain), and RNM-282 research group from the Junta de Andalucía (Spain).

Conflicts of Interest: The authors declare no conflict of interest.

References

1. Papa, F.; Prigent, C.; Rossow, W.B. Monitoring Flood and Discharge Variations in the Large Siberian Rivers from a Multi-Satellite Technique. *Surv. Geophys.* **2008**, *29*, 297–317. [CrossRef]
2. Brisco, B. Mapping and Monitoring Surface Water and Wetlands with Synthetic Aperture Radar. In *Remote Sensing of Wetlands: Applications and Advances*; CRC Press: Boca Raton, FL, USA, 2015; pp. 119–135.
3. Ji, L.; Zhang, L.; Wylie, B. Analysis of Dynamic Thresholds for the Normalized Difference Water Index. *Photogramm. Eng. Remote Sens.* **2009**, *11*, 1307–1317. [CrossRef]
4. Ozesmi, S.L.; Bauer, M.E. Satellite remote sensing of wetlands. *Wetl. Ecol. Manag.* **2002**, *10*, 381–402. [CrossRef]
5. Hung, M.C.; Wu, Y.H. Mapping and visualizing the Great Salt Lake landscape dynamics using multi-temporal satellite images, 1972–1996. *Int. J. Remote Sens.* **2005**, *26*, 1815–1834. [CrossRef]
6. Lira, J. Segmentation and morphology of open water bodies from multispectral images. *Int. J. Remote Sens.* **2006**, *27*, 4015–4038. [CrossRef]
7. Rogers, A.S.; Kearney, M.S. Reducing signature variability in unmixing coastal marsh Thematic Mapper scenes using spectral indices. *Int. J. Remote Sens.* **2004**, *25*, 2317–2335. [CrossRef]
8. Sethre, P.R.; Rundquist, B.C.; Todhunter, P.E. Remote Detection of Prairie Pothole Ponds in the Devils Lake Basin, North Dakota. *GIScience Remote Sens.* **2005**, *42*, 277–296. [CrossRef]
9. Bryant, R.G.; Rainey, M.P. Investigation of flood inundation on playas within the Zone of Chotts, using a time-series of AVHRR. *Remote Sens. Environ.* **2002**, *82*, 360–375. [CrossRef]
10. Jain, S.K.; Singh, R.D.; Jain, M.K.; Lohani, A.K. Delineation of Flood-Prone Areas Using Remote Sensing Techniques. *Water Resour. Manag.* **2005**, *19*, 333–347. [CrossRef]
11. McFeeters, S.K. The use of the Normalized Difference Water Index (NDWI) in the delineation of open water features. *Int. J. Remote Sens.* **1996**, *17*, 1425–1432. [CrossRef]
12. Xu, H. Modification of normalised difference water index (NDWI) to enhance open water features in remotely sensed imagery. *Int. J. Remote Sens.* **2006**, *27*, 3025–3033. [CrossRef]
13. Lacaux, J.P.; Tourre, Y.M.; Vignolles, C.; Ndione, J.A.; Lafaye, M. Classification of ponds from high-spatial resolution remote sensing: Application to Rift Valley Fever epidemics in Senegal. *Remote Sens. Environ.* **2007**, *106*, 66–74. [CrossRef]
14. Shen, L.; Li, C. Water body extraction from Landsat ETM+ imagery using adaboost algorithm. In Proceedings of the 2010 18th International Conference on Geoinformatics, Beijing, China, 18–20 June 2010; pp. 1–4.
15. Feyisa, G.L.; Meilby, H.; Fensholt, R.; Proud, S.R. Automated Water Extraction Index: A new technique for surface water mapping using Landsat imagery. *Remote Sens. Environ.* **2014**, *140*, 23–35. [CrossRef]
16. Hoberg, T.; Rottensteiner, F.; Feitosa, R.Q.; Heipke, C. Conditional Random Fields for Multitemporal and Multiscale Classification of Optical Satellite Imagery. *IEEE Trans. Geosci. Remote Sens.* **2015**, *53*, 659–673. [CrossRef]
17. Fisher, A.; Flood, N.; Danaher, T. Comparing Landsat water index methods for automated water classification in eastern Australia. *Remote Sens. Environ.* **2016**, *175*, 167–182. [CrossRef]
18. Malahlela, O.E. Inland waterbody mapping: Towards improving discrimination and extraction of inland surface water features. *Int. J. Remote Sens.* **2016**, *37*, 4574–4589. [CrossRef]
19. Jiang, Z.; Qi, J.; Su, S.; Zhang, Z.; Wu, J. Water body delineation using index composition and HIS transformation. *Int. J. Remote Sens.* **2012**, *33*, 3402–3421. [CrossRef]
20. Sheng, Y.; Shah, C.A.; Smith, L.C. Automated Image Registration for Hydrologic Change Detection in the Lake-Rich Arctic. *IEEE Geosci. Remote Sens. Lett.* **2008**, *5*, 414–418. [CrossRef]
21. Acharya, T.D.; Lee, D.H.; Yang, I.T.; Lee, J.K. Identification of Water Bodies in a Landsat 8 OLI Image Using a J48 Decision Tree. *Sensors* **2016**, *16*, 1075. [CrossRef]

22. Olthof, I. Mapping Seasonal Inundation Frequency (1985–2016) along the St-John River, New Brunswick, Canada using the Landsat Archive. *Remote Sens.* **2017**, *9*, 143. [CrossRef]
23. Ryu, J.-H.; Won, J.-S.; Min, K.D. Waterline extraction from Landsat TM data in a tidal flat: A case study in Gomso Bay, Korea. *Remote Sens. Environ.* **2002**, *83*, 442–456. [CrossRef]
24. Du, Z.; Li, W.; Zhou, D.; Tian, L.; Ling, F.; Wang, H.; Gui, Y.; Sun, B. Analysis of Landsat-8 OLI imagery for land surface water mapping. *Remote Sens. Lett.* **2014**, *5*, 672–681. [CrossRef]
25. Singh, K.V.; Setia, R.; Sahoo, S.; Prasad, A.; Pateriya, B. Evaluation of NDWI and MNDWI for assessment of waterlogging by integrating digital elevation model and groundwater level. *Geocarto Int.* **2015**, *30*, 650–661. [CrossRef]
26. Gulácsi, A.; Kovács, F. Sentinel-1-Imagery-Based High-Resolution Water Cover Detection on Wetlands, Aided by Google Earth Engine. *Remote Sens.* **2020**, *12*, 1614. [CrossRef]
27. Manjusree, P.; Kumar, L.P.; Bhatt, C.M.; Rao, G.S.; Bhanumurthy, V. Optimization of threshold ranges for rapid flood inundation mapping by evaluating backscatter profiles of high incidence angle SAR images. *Int. J. Disaster Risk Sci.* **2012**, *3*, 113–122. [CrossRef]
28. Hanssen, R.F. *Radar Interferometry: Data Interpretation and Error Analysis*; Kluwer Academic Publishers: Dordrecht, The Netherlands, 2001; Volume 2, p. 308.
29. Bioresita, F.; Puissant, A.; Stumpf, A.; Malet, J.-P. A Method for Automatic and Rapid Mapping of Water Surfaces from Sentinel-1 Imagery. *Remote Sens.* **2018**, *10*, 217. [CrossRef]
30. Twele, A.; Cao, W.; Plank, S.; Martinis, S. Sentinel-1-based flood mapping: A fully automated processing chain. *Int. J. Remote Sens.* **2016**, *37*, 2990–3004. [CrossRef]
31. Huang, W.; DeVries, B.; Huang, C.; Lang, M.W.; Jones, J.W.; Creed, I.F.; Carroll, M.L. Automated Extraction of Surface Water Extent from Sentinel-1 Data. *Remote Sens.* **2018**, *10*, 797. [CrossRef]
32. Amitrano, D.; Martino, G.D.; Iodice, A.; Mitidieri, F.; Papa, M.N.; Riccio, D.; Ruello, G. Sentinel-1 for Monitoring Reservoirs: A Performance Analysis. *Remote Sens.* **2014**, *6*, 10676–10693. [CrossRef]
33. Ezzahar, J.; Ouaadi, N.; Zribi, M.; Elfarkh, J.; Aouade, G.; Khabba, S.; Er-Raki, S.; Chehbouni, A.; Jarlan, L. Evaluation of Backscattering Models and Support Vector Machine for the Retrieval of Bare Soil Moisture from Sentinel-1 Data. *Remote Sens.* **2020**, *12*, 72. [CrossRef]
34. Shang, J.; Liu, J.; Poncos, V.; Geng, X.; Qian, B.; Chen, Q.; Dong, T.; Macdonald, D.; Martin, T.; Kovacs, J.; et al. Detection of Crop Seeding and Harvest through Analysis of Time-Series Sentinel-1 Interferometric SAR Data. *Remote Sens.* **2020**, *12*, 1551. [CrossRef]
35. Liang, J.; Liu, D. A local thresholding approach to flood water delineation using Sentinel-1 SAR imagery. *ISPRS J. Photogramm. Remote Sens.* **2020**, *159*, 53–62. [CrossRef]
36. Martinis, S.; Twele, A.; Voigt, S. Towards operational near real-time flood detection using a split-based automatic thresholding procedure on high resolution TerraSAR-X data. *Nat. Hazards Earth Syst. Sci.* **2009**, *9*, 303–314. [CrossRef]
37. Su, Z.; Troch, P.A.; De Troch, F.P. Remote sensing of bare surface soil moisture using EMAC/ESAR data. *Int. J. Remote Sens.* **1997**, *18*, 2105–2124. [CrossRef]
38. Schmugge, T.; Jackson, T. Passive Microwave Remote Sensing of Soil Moisture. In *Land Surface Processes in Hydrology*; Springer: Berlin/Heidelberg, Germany, 1997; pp. 239–262.
39. Altese, E.; Bolognani, O.; Mancini, M.; Troch, P.A. Retrieving Soil Moisture Over Bare Soil from ERS 1 Synthetic Aperture Radar Data: Sensitivity Analysis Based on a Theoretical Surface Scattering Model and Field Data. *Water Resour. Res.* **1996**, *32*, 653–661. [CrossRef]
40. Ulaby, F.T.; Aslam, A.; Dobson, M.C. Effects of Vegetation Cover on the Radar Sensitivity to Soil Moisture. *IEEE Trans. Geosci. Remote Sens.* **1982**, *GE-20*, 476–481. [CrossRef]
41. Fung, A.K.; Li, Z.; Chen, K.S. Backscattering from a randomly rough dielectric surface. *IEEE Trans. Geosci. Remote Sens.* **1992**, *30*, 356–369. [CrossRef]
42. Filipponi, F. Sentinel-1 GRD Preprocessing Workflow. *Proceedings* **2019**, *18*, 11.
43. Sinha, N.K.; Shokr, M. *Sea Ice: Physics and Remote Sensing*; John Wiley & Sons: Hoboken, NJ, USA, 2015; p. 600.
44. Gorelick, N.; Hancher, M.; Dixon, M.; Ilyushchenko, S.; Thau, D.; Moore, R. Google Earth Engine: Planetary-scale geospatial analysis for everyone. *Remote Sens. Environ.* **2017**, *202*, 18–27. [CrossRef]
45. Pereira, M. *Relatório de Elaboração da CAV. ANA CAV—Açudes. Lote 02—Açude Poço da Cruz*; ANA—Agência Nacional de Águas: Brasília, Brazil, 2018; p. 98.
46. Pham-Duc, B.; Prigent, C.; Aires, F. Surface Water Monitoring within Cambodia and the Vietnamese Mekong Delta over a Year, with Sentinel-1 SAR Observations. *Water* **2017**, *9*, 366. [CrossRef]
47. Embrapa. Vegetation Temporal Analysis System (SATVeg). Available online: www.satveg.cnptia.embrapa.br (accessed on 22 February 2021).
48. Esquerdo, J.C.D.M.; Antunes, J.F.G.; Coutinho, A.C.; Speranza, E.A.; Kondo, A.A.; dos Santos, J.L. SATVeg: A web-based tool for visualization of MODIS vegetation indices in South America. *Comput. Electron. Agric.* **2020**, *175*, 105516. [CrossRef]
49. Grinsted, A.; Moore, J.C.; Jevrejeva, S. Application of the cross wavelet transform and wavelet coherence to geophysical time series. *Nonlin. Processes Geophys.* **2004**, *11*, 561–566. [CrossRef]
50. Maraun, D.; Kurths, J. Cross wavelet analysis: Significance testing and pitfalls. *Nonliner Process. Geophys.* **2004**, *11*, 505–514. [CrossRef]

51. Gouhier, T.; Grinsted, A.; Simko, V. R Package Biwavelet: Conduct Univariate and Bivariate Wavelet Analyses (Version 0.20.19). 2019. Available online: https://github.com/tgouhier/biwavelet (accessed on 21 March 2022).
52. Hijmans, R.J. *Raster: Geographic Data Analysis and Modeling*; CRAN: Vienna, Austria, 2020.
53. Wickham, H. *Ggplot2: Elegant Graphics for Data Analysis*; Springer: New York, NY, USA, 2016.
54. Pebesma, E. Simple Features for R: Standardized Support for Spatial Vector Data. *R J.* **2018**, *10*, 439–446. [CrossRef]
55. Famiglietti James, S.; Rodell, M. Water in the Balance. *Science* **2013**, *340*, 1300–1301. [CrossRef]
56. Benninga, H.-J.F.; van der Velde, R.; Su, Z. Sentinel-1 soil moisture content and its uncertainty over sparsely vegetated fields. *J. Hydrol. X* **2020**, *9*, 100066. [CrossRef]
57. Theis, S.W.; Blanchard, B.J.; Newton, R.W. Utilization of vegetation indices to improve microwave soil moisture estimates over agricultural lands. *IEEE Trans. Geosci. Remote Sens.* **1984**, *GE-22*, 490–496. [CrossRef]
58. Van Leeuwen, B.; Tobak, Z.; Kovács, F. Sentinel-1 and -2 Based near Real Time Inland Excess Water Mapping for Optimized Water Management. *Sustainability* **2020**, *12*, 2854. [CrossRef]
59. Weekley, D.; Li, X. Tracking Multidecadal Lake Water Dynamics with Landsat Imagery and Topography/Bathymetry. *Water Resour. Res.* **2019**, *55*, 8350–8367. [CrossRef]
60. Özelkan, E. Water Body Detection Analysis Using NDWI Indices Derived from Landsat-8 OLI. *Pol. J. Environ. Stud.* **2020**, *29*, 1759–1769. [CrossRef]
61. Bolanos, S.; Stiff, D.; Brisco, B.; Pietroniro, A. Operational Surface Water Detection and Monitoring Using Radarsat 2. *Remote Sens.* **2016**, *8*, 285. [CrossRef]
62. Reis, L.G.; Souza, W.D.; Ribeiro Neto, A.; Fragoso, C.R.; Ruiz-Armenteros, A.M.; Cabral, J.J.; Montenegro, S.M. Uncertainties Involved in the Use of Thresholds for the Detection of Water Bodies in Multitemporal Analysis from Landsat-8 and Sentinel-2 Images. *Sensors* **2021**, *21*, 7494. [CrossRef] [PubMed]